Acta Biomaterialia 171 (2023) 166–192

Contents lists available at ScienceDirect

Acta Biomaterialia

journal homepage: www.elsevier.com/locate/actbio

Full length article

Quantifying the microstructural and biomechanical changes in the porcine ventricles during growth and remodelling

Faizan Ahmad[a,b,*], Shwe Soe[c], Julie Albon[d,e], Rachel Errington[f], Peter Theobald[a,**]

[a] School of Engineering, Cardiff University, UK
[b] School of Health Sciences, Birmingham City University, UK
[c] FET - Engineering, Design and Mathematics, University of West of England, UK
[d] School of Optometry and Vision Sciences, Cardiff University, UK
[e] Viva Scientia Bioimaging Laboratories, Cardiff University, UK
[f] School of Medicine, Cardiff University, UK

ARTICLE INFO

Article history:
Received 23 February 2023
Revised 19 September 2023
Accepted 26 September 2023
Available online 4 October 2023

Keywords:
Cardiac-ageing
Biaxial properties of ventricles
Cardiac growth and remodelling
Viscoelastic properties of ventricles
Cardiomyocytes rotation and dispersion
Collagens rotation and dispersion
Biomechanical changes during G & R
Microstructural changes during G & R

ABSTRACT

Cardiac tissue growth and remodelling (G & R) occur in response to the changing physiological demands of the heart after birth. The early shift to pulmonary circulation produces an immediate increase in ventricular workload, causing microstructural and biomechanical changes that serve to maintain overall physiological homoeostasis. Such cardiac G & R continues throughout life. Quantifying the tissue's mechanical and microstructural changes because of G & R is of increasing interest, dovetailing with the emerging fields of personalised and precision solutions. This study aimed to determine equibiaxial, and non-equibiaxial extension, stress-relaxation, and the underlying microstructure of the passive porcine ventricles tissue at four time points spanning from neonatal to adulthood. The three-dimensional microstructure was investigated via two-photon excited fluorescence and second-harmonic generation microscopy on optically cleared tissues, describing the 3D orientation, rotation and dispersion of the cardiomyocytes and collagen fibrils. The results revealed that during biomechanical testing, myocardial ventricular tissue possessed non-linear, anisotropic, and viscoelastic behaviour. An increase in stiffness and viscoelasticity was noted for the left and right ventricular free walls from neonatal to adulthood. Microstructural analyses revealed concomitant increases in cardiomyocyte rotation and dispersion. This study provides baseline data, describing the biomechanical and microstructural changes in the left and right ventricular myocardial tissue during G & R, which should prove valuable to researchers in developing age-specific, constitutive models for more accurate computational simulations.

Statement of significance

There is a dearth of experimental data describing the growth and remodelling of left and right ventricular tissue. The published literature is fragmented, with data reported via different experimental techniques using tissues harvested from a variety of animals, with different gender and ages. This prevents developing a continuum of data spanning birth to death, so limiting the potential that can be leveraged to aid computational modelling and simulations. In this study, equibiaxial, non-equibiaxial, and stress–relaxation data are presented, describing directional-dependent material responses. The biomechanical data is consolidated with equivalent microstructural data, an important element for the development of future material models. Combined, these data describe microstructural and biomechanical changes in the ventricles, spanning G &R from neonatal to adulthood.

1. Introduction

Tissue growth and remodelling (G & R) enables the cardiac function to respond to ever-changing physiological demands. The early shift to pulmonary circulation [1,2] produces an immediate increase in workload [3,4] stimulating cardiomyocyte hypertrophy,

* Corresponding author at: School of Health Sciences, Birmingham City University, Seacole Building, City South Campus, Westbourne Rd, Birmingham B15 3TN, UK.
** Corresponding author at: Medical Engineering Research Group, Cardiff School of Engineering, Cardiff University, Queens Buildings, The Parade, Cardiff CF24 3AA, UK.
E-mail addresses: Faizan.Ahmad@bcu.ac.uk (F. Ahmad), TheobaldPS@cardiff.ac.uk (P. Theobald).

https://doi.org/10.1016/j.actbio.2023.09.044

hyperplasia, and extracellular collagen deposition [5,6]. The left ventricular porcine free-wall increases in mass 4.5-fold within the first 14 days, cell volume increases 3.5-fold, whilst cellular proliferation increases 2-fold [5]. Deposition of interstitial collagen also increases, peaking 15–20 days postnatal [6]. G & R eventually generates the structure and function typical of adult heart tissues [5,7,8] which, in porcine studies, increases the proportion of contractile versus fibrous elements [7,8]. Maturation also increases collagen fibril density, mono-nucleated and bi-nucleated cell concentrations [9,10], and increases collagen fibril crosslinking and assembly [11].

Tissue growth is triggered by increased stress and stretch in the cardiac tissue, initiating a new extracellular matrix (ECM) [12,13]. Tissue remodelling occurs through a change in ECM structure and composition [12–14]. Such a change in the organization, composition and assembly of the new ECM material causes an increase in biomechanical stiffness [15,16], and changes stress distribution and cardiac function [16]. For instance, ventricular wall functionality differs between neonates and adults, as the former can only increase the cardiac output by increasing the heart rate (although only limited), whereas the adult heart can also increase stroke volume [17,18]. Changes in stress are an important determinant during G & R, which may in part be responsible for the change in the cardiac structure across the myocardial wall [19,20]. Interestingly, the alterations in mechanical stress and stretch are the primary cause of collagen organization and alignment during G & R [21]. This alignment of the collagen fibres significantly contributes to tissue anisotropy, with an impact on the migration of other cells through the ECM [22].

Quantifying the tissue's mechanical behaviour because of G & R is of increasing interest, dovetailing with the emerging fields of personalised and precision medicine solutions. Various approaches to constituent modelling have been proposed to capture these behaviours, including stress [23,24], strain [25,26], and strain energy density [27,28]. Computational models of cardiovascular mechanics are increasingly used to simulate normal and pathophysiological conditions. Such models provide the opportunity to investigate the dynamics of myocardial strain and the estimation of local stresses, data that are impossible to collect experimentally [29,30]. Model relevance is dependant, however, on the ability to accurately simulate tissue behaviour. At its most simplistic, inputting the uniaxial mechanical tissue behaviour from a single region, applied 'globally' to the entire organ, enables simulations, though with limited accuracy. At the other extreme, tissue structure mapped across the organ, twinned with mechanical data describing multiple strain states and modes, will provide a true representation of the tissue's region-specific, non-linear, anisotropic behaviour.

Cardiac experimental studies have predominantly focused on adult tissue. Myocardium properties are typically reported from passive equi-biaxial extension tests [31–36], whilst Yin et al. [36] performed non-equibiaxial extension tests with different ratios, both using adult mongrel cardiac tissue. To determine the 'directional dependent' material response and 'cross coupling' of stress, it is important to apply different loading ratios along the two distinct planes, the mean fibre direction (MFD) and cross fibre direction (CFD) [37]. Sommer et al. [37] performed equi-and nonequi-biaxial tests on the left ventricle-free wall of the adult human myocardium. Ahmad et al. [15] reported the biomechanical and microstructural properties of neonatal porcine ventricle tissues. The region-specific, cross-directional, and cross-wall variations of passive biaxial mechanical properties for porcine and rat myocardial tissues have also been reported [38,39]. Whilst the passive myocardial behaviour has been studied extensively, the differences between the active and passive biomechanical behaviour produced at the fibre level to the organ-level function have recently been reported in the literature [40]. The relative variations in the left and right ventricles' biomechanical stiffness, anisotropy, and viscoelasticity have also been reported in the ovine hearts, due to differences in their embryologic origin, anatomy, and function [41–43]. The effects of G & R on biomechanical properties have been reported on other biological tissues, including pelvic tissues, aortic tissues, skin, tendons, coronary sinus tissues, and collateral ligaments [44–49]. All studies reported non-linear, anisotropic, and stiffer behaviour during G & R.

Three-dimensional imaging methodologies have been used to analyse the microstructure of myocardial tissue, including diffusion tensor imaging, magnetic resonance microscopy, micro-computed tomography, ultrasound techniques, and optical coherence tomography [50]. All these imaging modalities provide in-depth knowledge of the microstructural arrangements of cardiomyocytes. Two-photon excited fluorescence (TPEF) and second-harmonic generation (SHG) and confocal microscopy provide the opportunity to quantify both the cardiomyocyte and collagen fibrils microstructure that has been used to describe the three-dimensional cardiac microstructure of cardiomyocytes and collagen fibrils [51,52]. Techniques such as TPEF and SHG enable the optical sectioning of relatively thick tissue samples [53,54]. The former can image elastin and cardiomyocytes by exciting endogenous fluorophores, whilst SHG provides a deeper insight into those molecules lacking a centre of symmetry (e.g., collagen, microtubules, and myosin) [55,56]. Used in tandem, the two techniques provide a microscopic, 3D representation of the interplay between key proteins, resulting in the determination of orientation, rotation, and dispersion parameters throughout thicker tissue samples [37,51]. Applied to cardiac tissue, TPEF/SHG has revealed structural differences between adult and neonatal myocardial tissue [37,57]. Currently, despite knowledge of the structural and biomechanical changes during G & R, there is no experimental data available on the left and right ventricle myocardial tissues. The published literature remains fragmented, with data reported via different experimental techniques using tissues harvested from a variety of animals, with different gender and ages. This prevents developing a continuum of data spanning birth to death, limiting the potential that can currently be leveraged to aid computational modelling.

This study reports microstructural and biomechanical data from left and right ventricle-free walls (LVFW, RVFW). A porcine model – which is a widely accepted surrogate animal model in cardiac-related research [58–60], was used throughout, with tissue harvested from animals of different ages to broadly capture early, mid and later stages of life. A consistent experimental setup was adopted, allowing a direct comparison of results across this study.

2. Materials and methods

This study aims to provide the first dataset combining the microstructure and biomechanical properties of porcine myocardial tissue across 4 ages. TPEF/SHG was performed on cleared tissue, with adjacent samples exposed to equi-biaxial, non-equibiaxial and stress relaxation testing.

2.1. Materials

Welsh porcine hearts (gilts or sows) were acquired from a local breeding farm. Twenty-five hearts ($N = 25$) were harvested from each age group (1 day, 14 days, 7 months, and 3 years old), totalling 100 hearts. A heart from each age is presented for comparison in Fig. 1 (a–d). All animals were slaughtered for the food industry except the youngest, where the piglet most likely died due to hypoxia either during or immediately after, farrowing (i.e., birth). All hearts appeared healthy and fully developed, with consistent tissue colour and no obvious abnormalities. Following removal, all hearts were submerged in 1000 ml cardioplegic solution

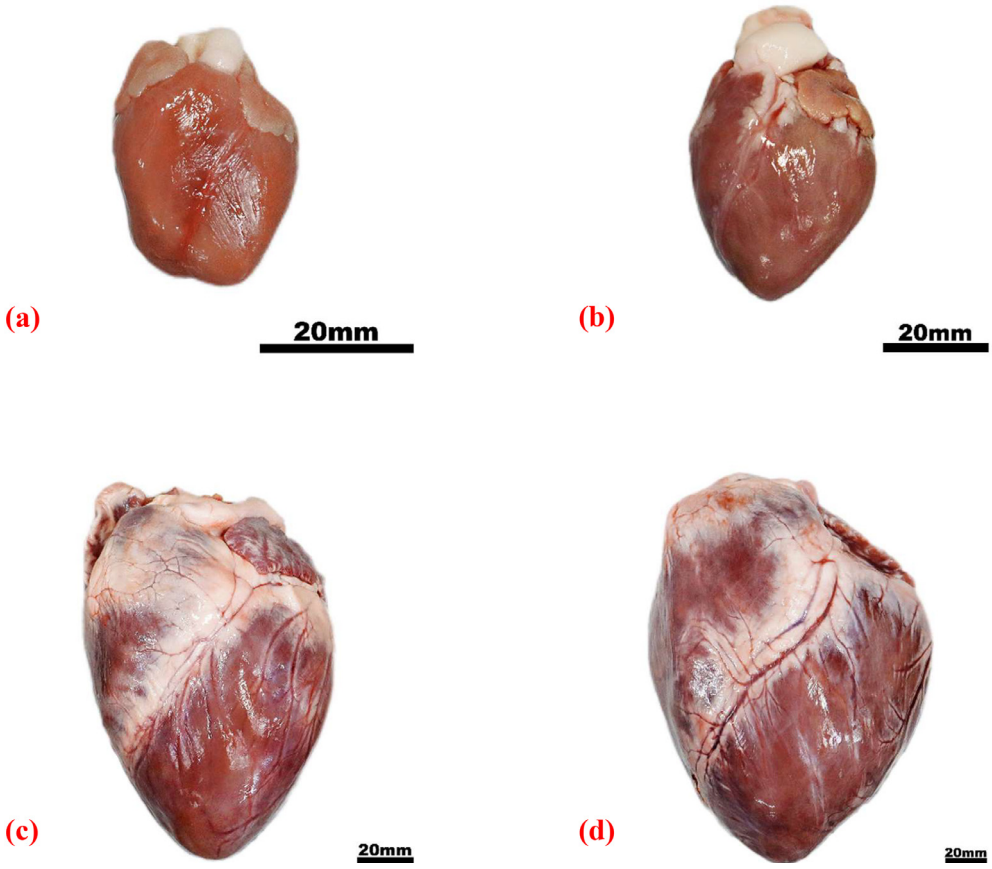

Fig. 1. Harvested porcine hearts of four age groups, namely 1 day old (a), 14 days old (b), 7 months old (c), and 3 years old (d). Scale bar = 20 mm. (e) 3D schematic model of the porcine ventricular myocardium composed of the right ventricular free wall (RVFW), highlighted with the blue region; the interventricular septum, highlighted with the purple region; and the left ventricular free wall (LVFW), highlighted with the red region. The local coordinates f_o, n_o, and s_o correspond to the mean fibre, cross fibre and sheetlet directions of the 'ellipsoidal' ventricles, respectively. (f) Squared specimens were dissected from the anterior aspect of the equatorial region of the RVFW and LVFW, to perform TPEF/SHG microscopic imaging through the absolute thickness (i.e., epicardium to endocardium). (g) Squared biaxial specimens were obtained from the anterior aspect of the equatorial region of the RVFW and LVFW. The square biaxial specimens were then aligned in the mean fibre direction (MFD) and cross fibre direction (CFD). (For interpretation of the references to colour in this figure legend, the reader is referred to the web version of this article.).

with dissolved 20 mM 2, 3-butanedione monoxime (BDM) immediately after the animals' slaughter (to inhibit cross-bridge activity and prevent any muscular contraction [37,61]), and stored at 4 °C. The LVFW and RVFW were then identified (Fig. 1e), before defining: the FSN-coordinate system as the fibre axis (f_o), defined as the mean-fibre direction as observed by the external surface texture; the sheet axis (s_o), defined as the direction transverse to the fibre axis within the layer, and; the sheet-normal axis (n_o), defined as the direction perpendicular to both the fibres and layer, as depicted in Fig. 1e [37,61]. In this study, the fibre axis (f_o) is described as the 'mean-fibre direction' (MFD), and the sheet-normal axis (n_o) as the 'cross fibre direction' (CFD). These coordinate axes were arranged in a manner consistent with previous heart biomechanical studies [15,37,61]. Biomechanical testing was completed within 12 h of the animal's death, to produce data from fresh tissue. The use of animal tissue was approved by the Department of Environment, Food, and Rural Affairs (DEFRA) - Animal & Plant Health Agency, UK (ABP registration reference: U1251982/ABP/OTHER).

2.2. Methods

2.2.1. Microstructural investigations

TPEF/SHG sample preparation: The LVFW and RVFW specimens were dissected from the equatorial (mid) region across all age groups, as shown in Fig. 1(f). A reference axis was defined as passing through the apex and base, with the edge of a 15 × 15 mm square cutter kept parallel to this axis when dissecting tissue samples, taken through the ventricle walls (Fig. 1f). The defined reference axis (apex-to-base) is considered 0° for all imaging Z-stacks. To image through the entire ventricle thickness (i.e., epicardium to endocardium), the walls were sectioned to multiple thin specimens of 200 µm, via a sledge microtome (HM440E + K400 (Mircrom)).

Optical clearing of heart tissues: Samples were fixed with 4 % paraformaldehyde (PFA) for 12 h, to achieve sufficient fixation. The myocardial samples were then rinsed with phosphate-buffered saline to wash off the PFA, then dehydrated using a graded ethanol series with each step lasting 2 h, according to the following protocol: 50 % 70 %, twice at 95 % and twice at 100 % [62]. For optical clearing, a solution of 1:2 benzyl alcohol: benzyl benzoate (BABB) was used. Each sample was initially submerged into a solution of 1:1 ethanol: BABB for 12 h before submerging into a 100 % BABB solution, where they remained clear for at least 24 h before imaging [62]. All steps involved in the tissue preparation, fixation and optical clearing were performed at room temperature.

TPEF/SHG Image Acquisition: Tissue samples were mounted onto coverslips (VWR Scientific Inc) and immersed in wintergreen oil (mountant). TPEF/SHG images were acquired by non-linear microscopy (NLM), using a laser scanning microscope (LSM880 NLO, Carl Zeiss, Ltd. Cambridge, UK) equipped with an ultrafast-pulsed, near-infrared TiS laser illumination system (Chameleon Vision II, Coherent Lasers, Cambridge, UK). Laser excitation at 900 nm and an approximate 140 fs pulse width were used for all NLM imaging, which was passed to the specimen and separated from returning emissions by a 690 nm short-pass primary dichroic reflector [57].

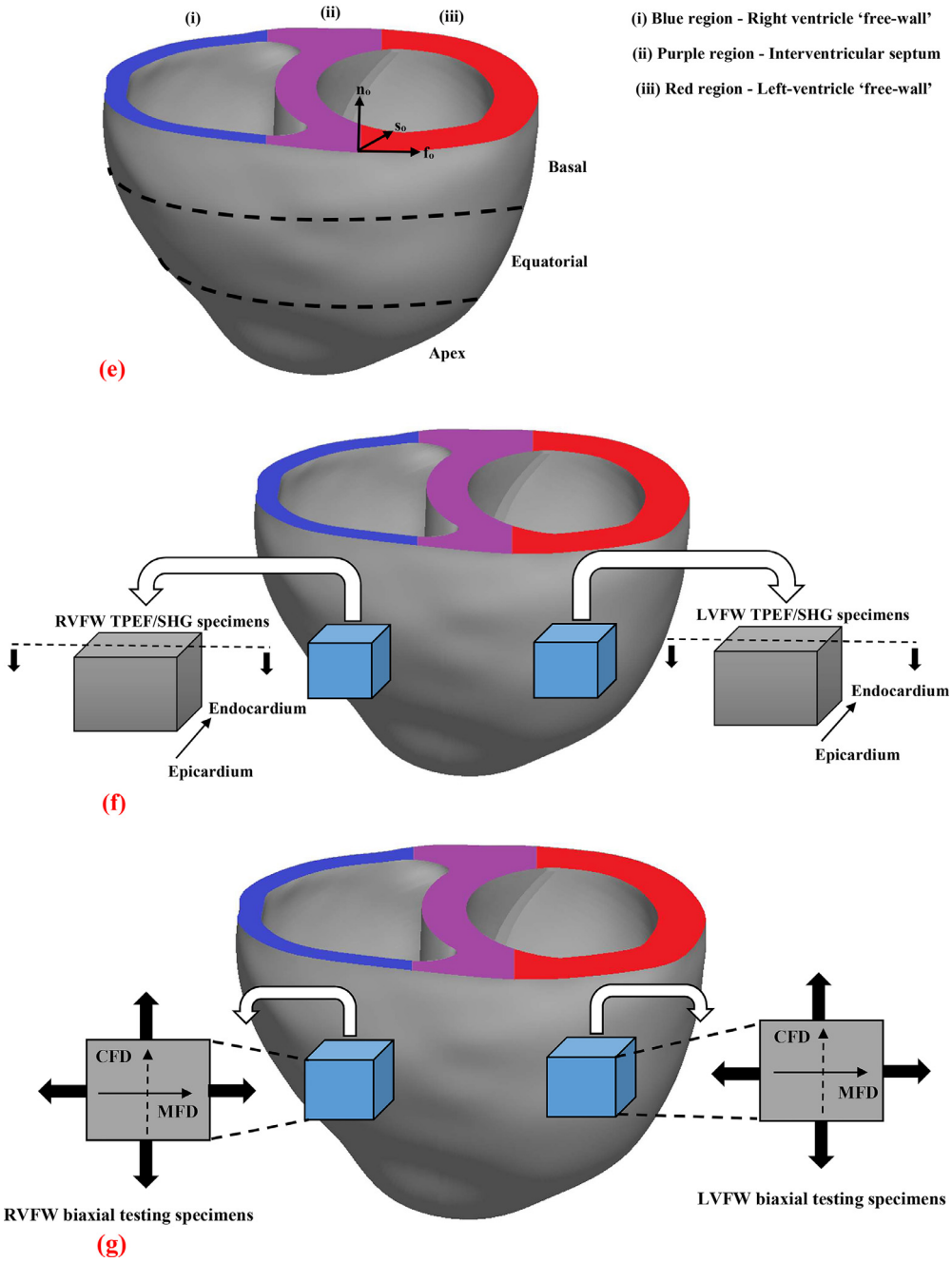

Fig. 1. Continued

All NLM imaging was performed using this technique via an objective lens (Plan-Apochromat 63x/1.40 Oil Ph3, Zeiss). Backwards-propagating TPEF and SHG light from the specimen was collected by the objective and detected in the reflected light (epi–) pathway of the microscope, using the internal spectrometer to select the desired wavelengths. SHG (at half the excitation wavelength) was detected at 450 ± 10 nm and TPEF at all wavelengths longer than 470 nm [57].

Two-channel (TPEF and SHG), 8-bit images were acquired simultaneously at serial focal positions to build up a 3D stack of optical sections collected at 1.52 µs. This comprised in-plane (x, y) stacks, with a field of view of 1024 × 1024 µm. Each line of every 2D optical section was scanned 16 times and the average signal was recorded. The laser power during the acquisition of deeper images was automatically increased following a pre-set pattern, to compensate for light scattering reducing the illumination.

2.2.2. Mechanical testing

Custom-built biaxial testing system: A biaxial testing system was used to perform equi-and non-equibiaxial tests on soft biological tissues (Fig. 2). Briefly, the testing system comprises 4 stepper motor-based linear slides - with integrated displacement control (EAS2NX-E015-AZAKD-3 – Oriental Motors LTD, Basingstoke UK), placed orthogonally to each other (Fig. 2). Two load cells (DBCR-10N-002-000 – Applied Measurements LTD, Berkshire UK) are attached to the X (MFD) and Y (CFD) axes of the testing system (Fig. 2). A water bath allows submerging of the tissue in physiological solution at 37 °C (Fig. 2). In-house LabVIEW (National Instruments Corporation, Texas US) code was developed for sending

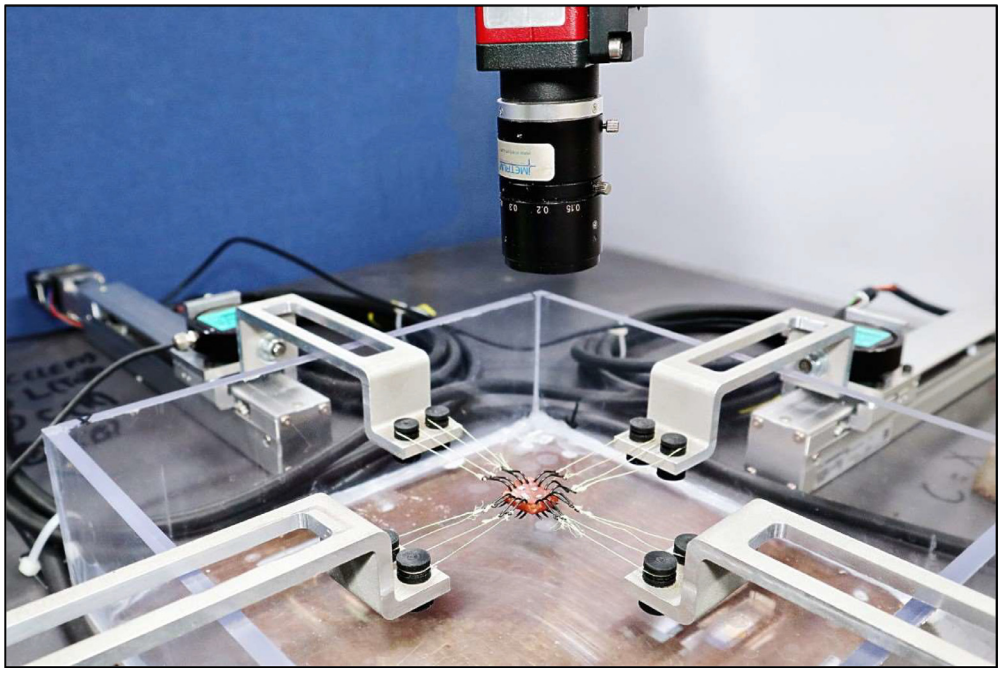

Fig. 2. Custom-built biaxial testing system, consisting of four linear actuator platforms, two load cells aligned in the MFD and CFD, a heated container, and the video extensometer camera for non-contact deformation measurements. A squared porcine myocardium specimen for biaxial extension testing with sides aligned with the MFD and CFD. White dots were placed in the middle of the specimen to be used as deformation markers. Surgical sutures attached to hooks were used to stretch the biaxial specimen.

simultaneous Input/Output digital signals to the stepper motors, to start the operation according to pre-programmed commands, saved in their drivers (MEXE02 Product Support Software - Oriental Motor USA Corp). Non-contact video-extensometry (iMetrum CAM028; Bristol, UK) was used to track the displacement of markers adhered to the centre of the tissue samples. All data was captured via a National Instrument data acquisition system (NI myRIO-1900, National Instruments Corporation, Texas US). The biaxial testing system is illustrated in Fig. 2.

Specimen Preparation: The LVFW and RVFW specimens were dissected from the equatorial (mid) region of the porcine heart, as shown in Fig. 1g. Thin myocardial tissue slices with a consistent thickness and a smooth surface, were achieved using a universal cutter. From these thin slices, square 15 × 15 mm specimens were prepared using a modified toggle press (RS PRO 0.6t Manual Toggle Press, UK), with one side aligned with the MFD and the other in the CFD, as depicted in Fig. 1g [63]. In this study, the biaxial myocardial tissue specimen for the LVFW and RVFW were obtained from the outer portion of the wall. 'Outer' corresponds to specimens taken ~ 1.5–2.0 mm below the epicardial surface [37]. A detailed description of preparing suitable biaxial specimens has been provided elsewhere [63].

The specimens were then sutured onto the custom-built biaxial testing system and submerged in a bath of CPS with 20 mM BDM, which remained at 37 °C. Testing was performed at 37 °C in the presence of BDM, an inhibitor of cross-bridge cycling [37,64].

Equi-biaxial and non-equibiaxial extension protocol: Specimens were stretched from 2.5 % to 15 % in 2.5 % increments, starting with the smallest stretch. In each stretch level, five preconditioning cycles and one measuring cycle were performed at different loading ratios, including equi-and non-equibiaxial loading ratios (1(MFD):1(CFD), 0.75:1, 0.5:1, 1:0.75, 1:0.5) [37]. Loading and unloading curves were obtained within each measuring cycle.

Stress relaxation protocol: Stress relaxation tests (Cauchy stresses vs. time) were performed to quantify any viscoelastic changes in the LVFW and RVFW, at a ramp speed of 100 mm/min for the stretch level of 10 %, for 300 s [37].

2.3. Data analysis

2.3.1. Microstructural analysis

Tissue microstructure is typically characterised by quantifying fibre orientation, rotation, and dispersion from TPEF/SHG imaging. Fiji/Image J (NIH, USA) software was used to perform quantitative analysis on TPEF/SHG image Z-stacks. In-plane (x, y) images were pre-processed in three dimensions using selected computational filters (unsharp mask, Gaussian blur 3D and Kuwahara) before these 'stacks' were analysed using the Fourier components analysis method [65]. This approach enabled quantification of the collagen and cardiomyocyte distributions, relative to the stack depth. Using the ImageJ plug-in 'Directionality' (https://imagej.net/Directionality), data from all images within the stacks were used to generate a histogram. The peak was then fitted to a Gaussian function, enabling the identification of the preferred fibre orientation direction and subsequent rotation, a method consistent with other studies [57,66,67]. The output comprised: (1) the preferred fibre orientation direction (°), defined by the centre of the Gaussian distribution; (2) the angular dispersion (°), defined as the standard deviation (std) of the Gaussian distribution; (3) the amount parameter, defined as the sum of the histogram from minus 1 std to plus 1 std, divided by the total sum of the histogram; (4) goodness of fit (R^2). TPEF/SHG images with $R^2 > 0.8$ were used for further analyses, an identical threshold to that adopted elsewhere [37,57].

2.3.2. Mechanical testing

Cauchy stress vs. stretch was plotted to understand tissue behaviour. It was assumed that there were negligible shear stresses during biaxial testing, as has been reported elsewhere [63]. Also, the methodology adopted in this study, to align the myocardial tissue specimen in the MFD and CFD, results in negligible shear deformation and stresses. This approach has also been described elsewhere [37,63]. With the incompressibility assumption [68], the (normal) Cauchy stresses in MFD, σ_{11}, and CFD, σ_{22}, can be determined from the first Piola–Kirchhoff stresses in MFD, P_{11}, and CFD,

P_{22}, respectively [69]. Thus,

$$\sigma_{11} = \lambda_1 P_{11} = \lambda_1 \frac{f_1}{TL_2}, \sigma_{22} = \lambda_2 P_{22} = \lambda_1 \frac{f_2}{TL_1}, \quad (1)$$

where $\lambda_1 = x_1/X_1$ and $\lambda_2 = x_2/X_2$ represent the tissue stretch in each direction, based on the marker distances in the loaded (x_1, x_2) and unloaded (X_1, X_2) configuration. The measured force in each direction is denoted as f_1 and f_2; T is the mean thickness in the unloaded reference configuration, and L_1 and L_2 are the measurable side lengths of the specimen in the undeformed state in the fibre and cross-fibre direction, respectively. In this study, L_1 and L_2 were approximately 15 mm.

The mechanical properties of LVFW and RVFW myocardial tissues were calculated and compared across all four age groups through extensibility (EXT), tangent modulus (TM), and degree of anisotropy (DA) in the MFD and CFD. From the equibiaxial testing protocol, the TM at two linear regions of the stress-strain curve, the low-load pre-transitional and high-load post-transitional regions, were calculated to provide a comparative measure of stiffness between the ventricle myocardial tissues across four age groups as demonstrated in [70]. The data points within each region were fitted in the least-square sense using a custom MATLAB code (MathWorks, Natick, MA). TM was calculated from the slope of the fitted line, and EXT was defined as the intersection of the fitted line with the x-axis. The EXT and TM parameters were calculated in MFD and CFD directions as shown in [70]. The DA values were calculated as the ratio of MFD to CFD strain at the maximum stress value under equibiaxial stress (T11: T22 = 1:1) [71]. A DA value of 1 indicates an isotropic material, while other values between 0 and 1 represent various degrees of anisotropy.

2.3.3. Statistical analyses

Biaxial data was averaged at each sampling point, with the variance informing the error bars. The overall non-linear trends were informed by data from each of these sampling points. The differences between the means of each sample group were quantified using a one-way analysis of variances (ANOVA), performed along with the Tukey HSD post hoc test for pair-wise multiple comparisons. Correlations between two variables were determined using Spearman (for non-parametric data) correlation coefficient (r), and p-values were calculated based on the statistical tests. All collected data are presented as a mean±standard error. A p-value less than 0.05 was considered statistically significant. Statistical analyses were performed using SPSS 20.0

3. Results

3.1. Microstructural analyses

TPEF/SHG microscopy was used to quantify the cardiomyocytes and interstitial collagen fibril's preferred orientation, rotation, and dispersion through the LVFW and RVFW thickness (i.e., epicardium to endocardium), across the four age groups. The SHG channel (green) identifies collagen fibril distribution and the TPEF channel (red), cardiomyocytes. Both channels were merged to demonstrate the collagen-cardiomyocyte overlapping as demonstrated in Fig. 3 (a–h). The cardiomyocytes and collagen fibrils exhibited a difference in rotation and dispersion between the young and adult myocardial tissues of both ventricles, as demonstrated in Fig.4 (a–d) & (g–j) and Fig. 5 (a–d) & (g–j) & (Tables 1 and 2).

Cardiomyocytes and collagen fibril rotation: In the LVFW, cardiomyocytes demonstrated a change in rotation across all four age groups, as demonstrated in Fig. 4a and g & Fig. 5a and g. Initially, it decreases from 1 to 14 days (145° vs. 64°), followed by an increase between 14 days and 7 months (64° vs. 402°) and finally decreases between 7 months to 3 years (402° vs. 250°), as described in Table 1. The greatest and smallest LVFW cardiomyocyte rotation was at 7 months and 14 days respectively (Table 1). LVFW collagen rotation increased with age (Fig.4a and g & Fig 5a and g), dramatically from 1 day to 14 days (136° vs. 417°), followed by a more modest increase from 14 days to 7 months (417° vs. 516°), and 7 months to 3 years (516° vs. 655°) (Table 1). In contrast to LVFW cardiomyocytes, the greatest and smallest LVFW collagen rotation was found at the age groups of 3 years and 1 day old respectively (Table 1). The amount (concentration) parameters for LVFW cardiomyocytes and collagens were reported in Fig. 4e and k & Fig. 5e and k and Table 1.

Table 1
In-plane (x-y) cardiomyocytes and collagen fibril rotation, dispersion, and amount through the *LVFW* (i.e., epicardium to endocardium) of the porcine heart at each age group, namely, 1 day, 14 days, 7 months, and 3 years old respectively.

LVFW	1 day	14 days	7 months	3 years
Cardiomyocytes				
Rotation (°)	**145 ± 11**	**64 ± 9**	**402 ± 20**	**250 ± 14**
Dispersion (°)	**132 ± 7**	**97 ± 5**	**335 ± 12**	**238 ± 10**
Amount	0.25 ± 0.01	0.22 ± 0.03	0.26 ± 0.01	0.24 ± 0.02
Collagens				
Rotation (°)	**136 ± 13**	**417 ± 8**	**516 ± 21**	**655 ± 19**
Dispersion (°)	**128 ± 6**	**455 ± 15**	**814 ± 27**	**880 ± 25**
Amount	0.38 ± 0.03	0.49 ± 0.02	0.45 ± 0.01	0.50 ± 0.02

Results are expressed as mean ± standard error ($n = 5$).
Bold - One-way analysis of variance (ANOVA) revealed statistical significance across all age groups within the LVFW $p < 0.05$.
Bold - One-way analysis of variance (ANOVA) revealed statistical significance between the equivalent age groups across the LVFW and RVFW $p < 0.05$.

Table 2
In-plane (x-y) cardiomyocytes and collagen fibril rotation, dispersion and amount through the ***RVFW*** (i.e., epicardium to endocardium) of the porcine heart at each age group, namely, 1 day, 14 days, 7 months and 3 years old respectively.

RVFW	1 day	14 days	7 months	3 years
Cardiomyocytes				
Rotation (°)	**234 ± 15**	**119 ± 13**	**241 ± 20**	**238 ± 19**
Dispersion (°)	**183 ± 9**	**82 ± 5**	**249 ± 8**	**235 ± 7**
Amount	0.44 ± 0.04	0.28 ± 0.02	0.26 ± 0.03	0.33 ± 0.03
Collagens				
Rotation (°)	**250 ± 23**	**365** ± 20	**433 ± 26**	**780 ± 30**
Dispersion (°)	**469 ± 23**	**572 ± 18**	**636 ± 26**	**973 ± 33**
Amount	0.61 ± 0.03	0.59 ± 0.04	0.49 ± 0.03	0.58 ± 0.02

Results are expressed as mean ± standard error ($n = 5$).
Bold - One-way analysis of variance (ANOVA) revealed statistical significance across all age groups within the LVFW $p < 0.05$.
Bold - One-way analysis of variance (ANOVA) revealed statistical significance between the equivalent age groups across the LVFW and RVFW $p < 0.05$.

In the RVFW, variation in cardiomyocyte rotation was evident across all age groups, as described in Fig.4b and h & Fig. 5b and h. Firstly, the RVFW cardiomyocyte rotation decreases from 1 day to 14 days (234° vs. 119°), then increases between 14 days to 7 months (119° vs. 241°), and finally decreases very slightly between 7 months to 3 years (241° vs. 238°), as reported in Table 2. The greatest and smallest RVFW cardiomyocyte rotation was found in the age groups of 7 months and 14 days respectively (Table 2). RVFW collagen rotation appears to increase with age (Fig. 4b and h & Fig 5b and h) and is consistent with the LVFW (Tables 1 and 2). RVFW collagen rotation increases gradually between 1 day to 14 days (250° vs. 365°) and 14 days to 7 months (365° vs. 433°) as reported in Table 2. However, a significant increase in the rotation occurred from 7 months to 3 years (433° vs. 780°) (Table 2). Contrary to RVFW cardiomyocytes, the greatest and smallest RVFW collagen rotation was found at the age groups of 3 years and 1-day-old porcine hearts respectively (Table 2). The amount (concentration) parameters for RVFW cardiomyocytes and collagens were

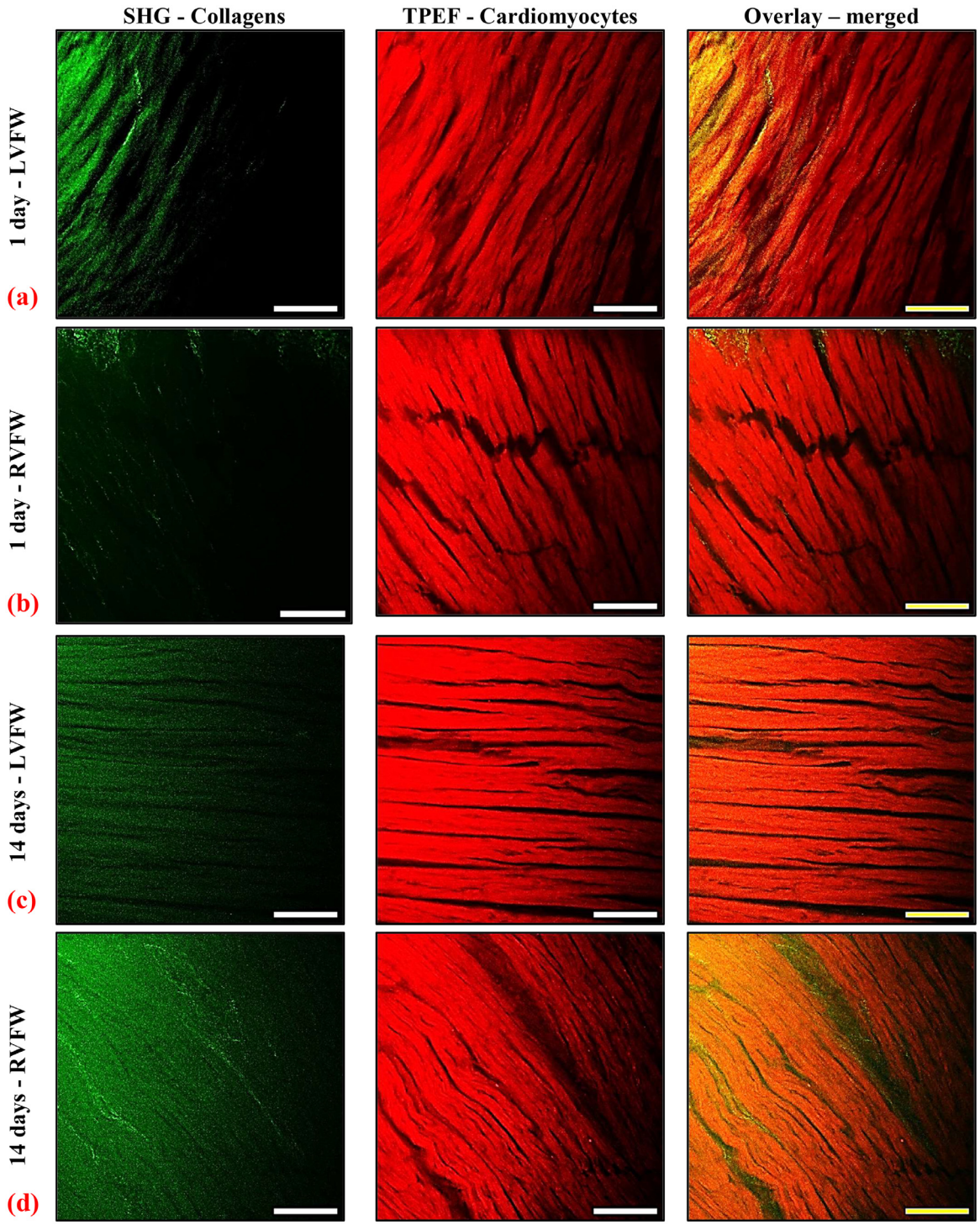

Fig. 3. In-plane TPEF/SHG representative images of the porcine LVFW and RVFW. Four age groups are presented namely, 1-day old LVFW (a) and RVFW (b); 14 days old LVFW (c) and RVFW (d); 7 months old LVFW (e) and RVFW (f); 3 years old LVFW (g) and RVFW (h). The SHG channel (green) identifies the collagen fibril distribution, and the TPEF channel (red) is the cardiomyocyte. Both channels were merged to demonstrate the collagen-cardiomyocyte overlapping. A reference axis was defined as passing through the apex and base, with the edge of a 15 × 15 mm square cutter kept parallel to this axis when dissecting tissue samples, taken through the ventricle walls. The defined reference axis (apex-to-base) is considered 0° for all imaging Z-stacks. Z-stacks were obtained through the absolute thickness of the LVFW and RVFW (i.e., epicardium to endocardium). Scale bar = 30 μm.(For interpretation of the references to colour in this figure legend, the reader is referred to the web version of this article.).

stated in Fig. 4f and l & Fig. 5f and l and Table 2. Statistical significance was found in rotation between the youngest and oldest tissues of all age groups within the LVFW and RVFW ($p < 0.05$), as stated in Tables 1 and 2.

Cardiomyocytes and collagen fibrils dispersion: LVFW cardiomyocytes exhibited a change in dispersion across all four age groups as demonstrated in Fig.4c and i & Fig. 5c and i. The cardiomyocyte dispersion decreases from 1 day to 14 days (132° vs. 97°), followed by an increase between 14 days to 7 months (97° vs. 335°), and finally, a decrease between 7 months to 3 years (335° vs. 238°) as reported in Table 1. The greatest and smallest LVFW cardiomyocyte dispersion was at 7 months and 14 days re-

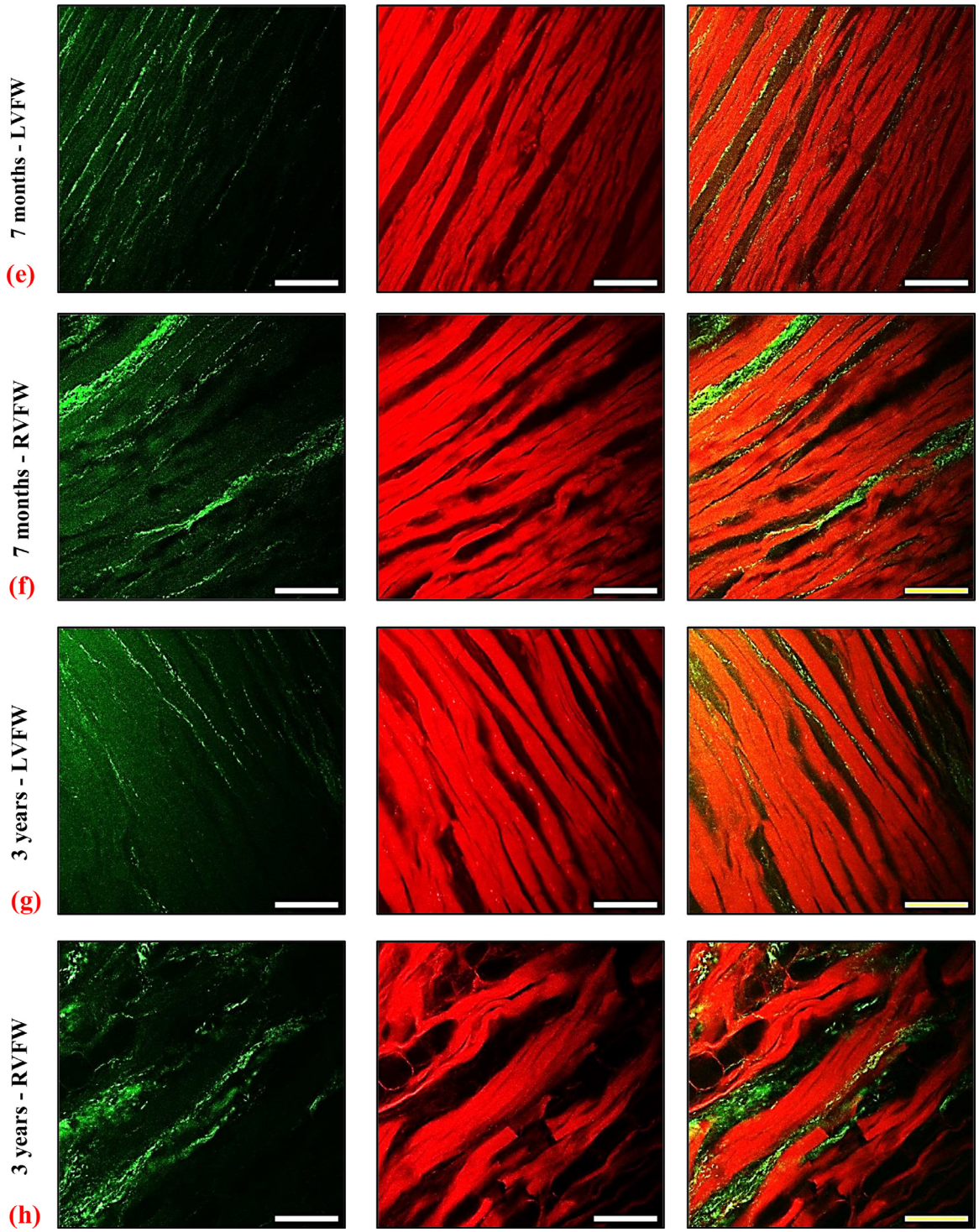

Fig. 3. Continued

spectively (Table 1). LVFW collagen dispersion increased with age, considerably between 1 day to 14 days (128° vs. 455°) and 14 days to 7 months (455° vs. 814°) (Table 1) and (Fig.4c and i & Fig. 5c and i). A more modest increase was observed between 7 months to 3 years (814° vs. 880°) (Table 1). In contrast to LVFW cardiomyocytes, the greatest and smallest LVFW collagens dispersion was found at the age groups of 3 years and 1 day respectively (Table 1).

In the RVFW, cardiomyocytes demonstrated a change in the dispersion with age, as described in Fig.4d and j & Fig. 5d and j. RVFW cardiomyocytes exhibited a decrease in dispersion from 1 day to 14 days (183° vs. 82°), followed by an increase between 14 days to 7 months (82° vs. 249°), and lastly decreasing slightly between 7 months to 3 years (249° vs. 235°) as described in Table 2. The greatest and smallest RVFW cardiomyocyte dispersion was found in the age groups of 7 months and 14 days respectively (Table 2). RVFW collagens exhibit an increase in dispersion with age (Fig.4d and j & Fig.5d and j). A relatively small increase was observed from 1 day to 14 days (469° vs. 572°) and 14 days to 7 months (572° vs. 636°) (Table 2), whilst a considerable increase in RVFW colla-

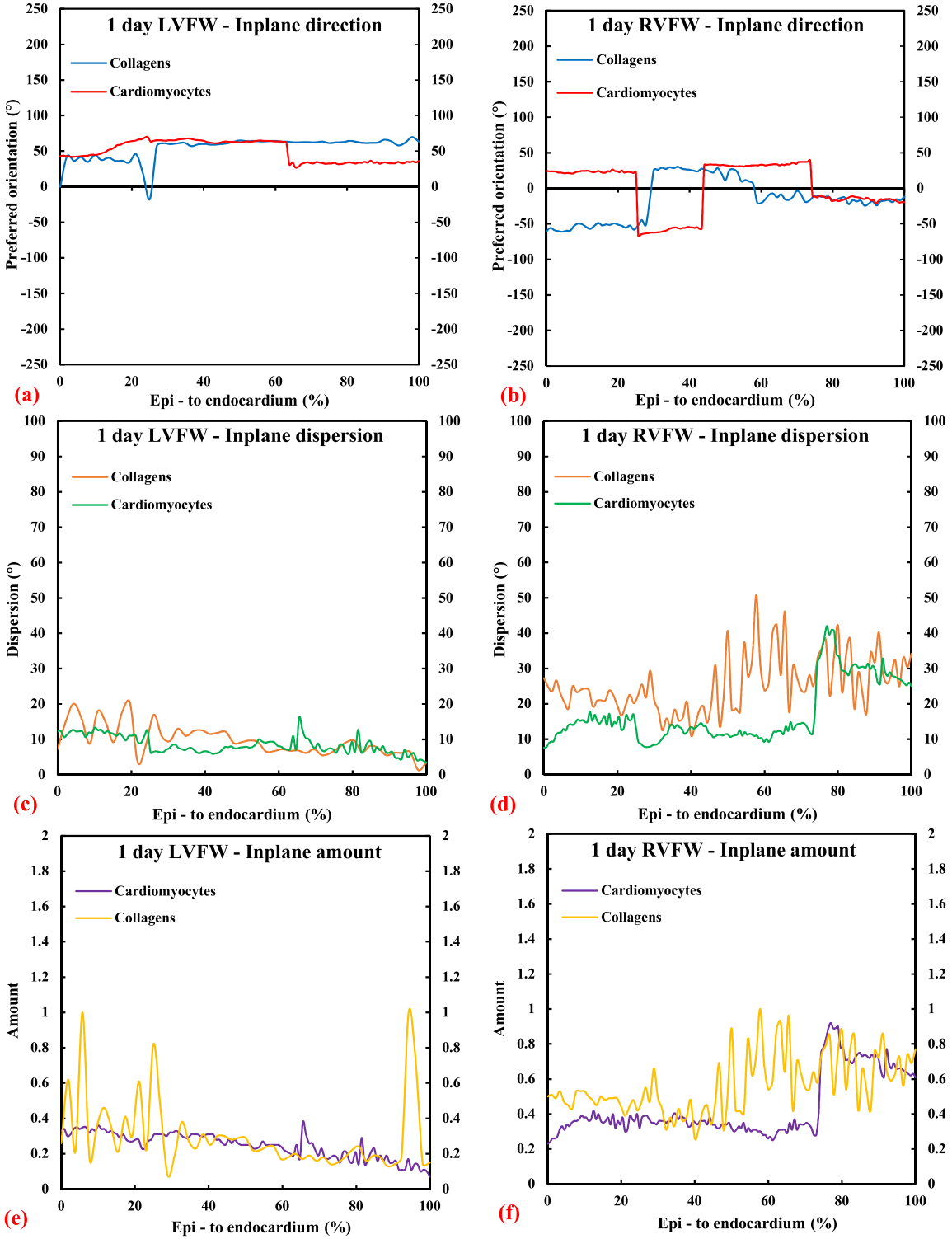

Fig. 4. TPEF/SHG microscopy was used to quantify the cardiomyocyte and collagen fibril microstructural parameters in the LVFW and RVFW ($n = 5$), consisting of in-plane preferred orientation, dispersion, and amount respectively. Microstructural data of two age groups are presented in this figure, namely, 1-day and 14 days old porcine hearts. ***1 day:*** (a) in-plane preferred orientation of 1-day LVFW; (b) in-plane preferred orientation of 1-day RVFW; (c) in-plane dispersion of 1-day LVFW; (d) in-plane dispersion of 1-day RVFW; (e) in-plane amount of 1-day LVFW; (f) in-plane amount of 1-day RVFW. ***14 days:*** (g) in-plane preferred orientation of 14-days LVFW; (h) in-plane preferred orientation of 14-days RVFW; (i) in-plane dispersion of 14-days LVFW; (j) in-plane dispersion of 14-days RVFW; (k) in-plane amount of 14-days LVFW; (l) in-plane amount of 14-days RVFW. In-plane image stacks were acquired through the absolute thickness of the LVFW and RVFW (i.e., epicardium to endocardium).

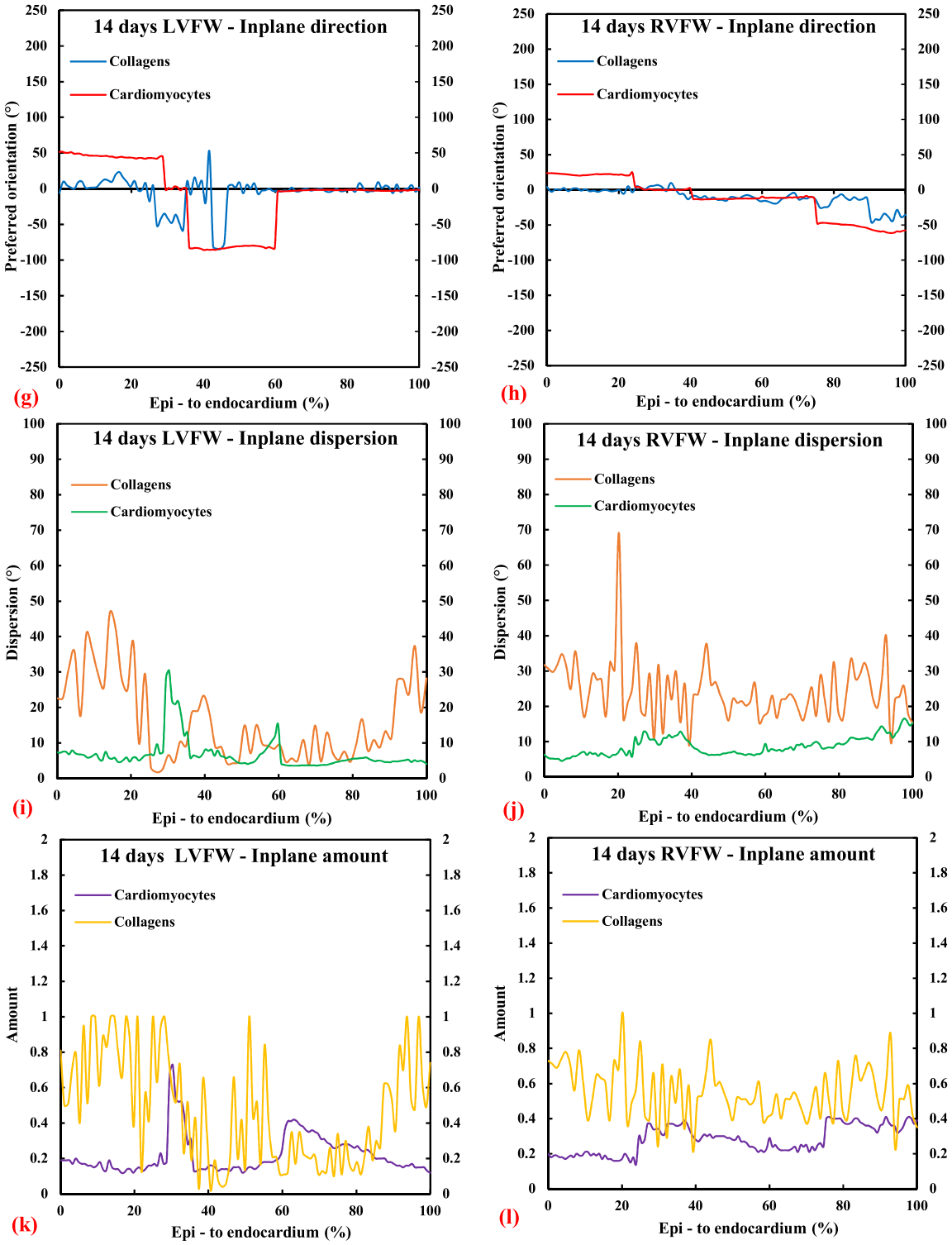

Fig. 4. Continued

gen dispersion was noted between 7 months and 3 years (636° vs. 973°) (Table 2). Contrary to cardiomyocytes, the greatest and smallest RVFW collagen dispersion was found at the age groups of 3 years and 1-day-old porcine hearts respectively (Table 2). Statistical significance was identified in rotation and dispersion between the equivalent age groups across the LVFW and RVFW ($p < 0.05$), as described in Tables 1 and 2.

3.2. Biaxial extension behaviour

The LVFW and RVFW possess non-linear, anisotropic, and viscoelastic biomechanical behaviour across all ages. The MFD is stiffer than the CFD. Hysteresis formation was pronounced during the preconditioning of the ventricular tissues, indicating the presence of energy dissipation per unit volume.

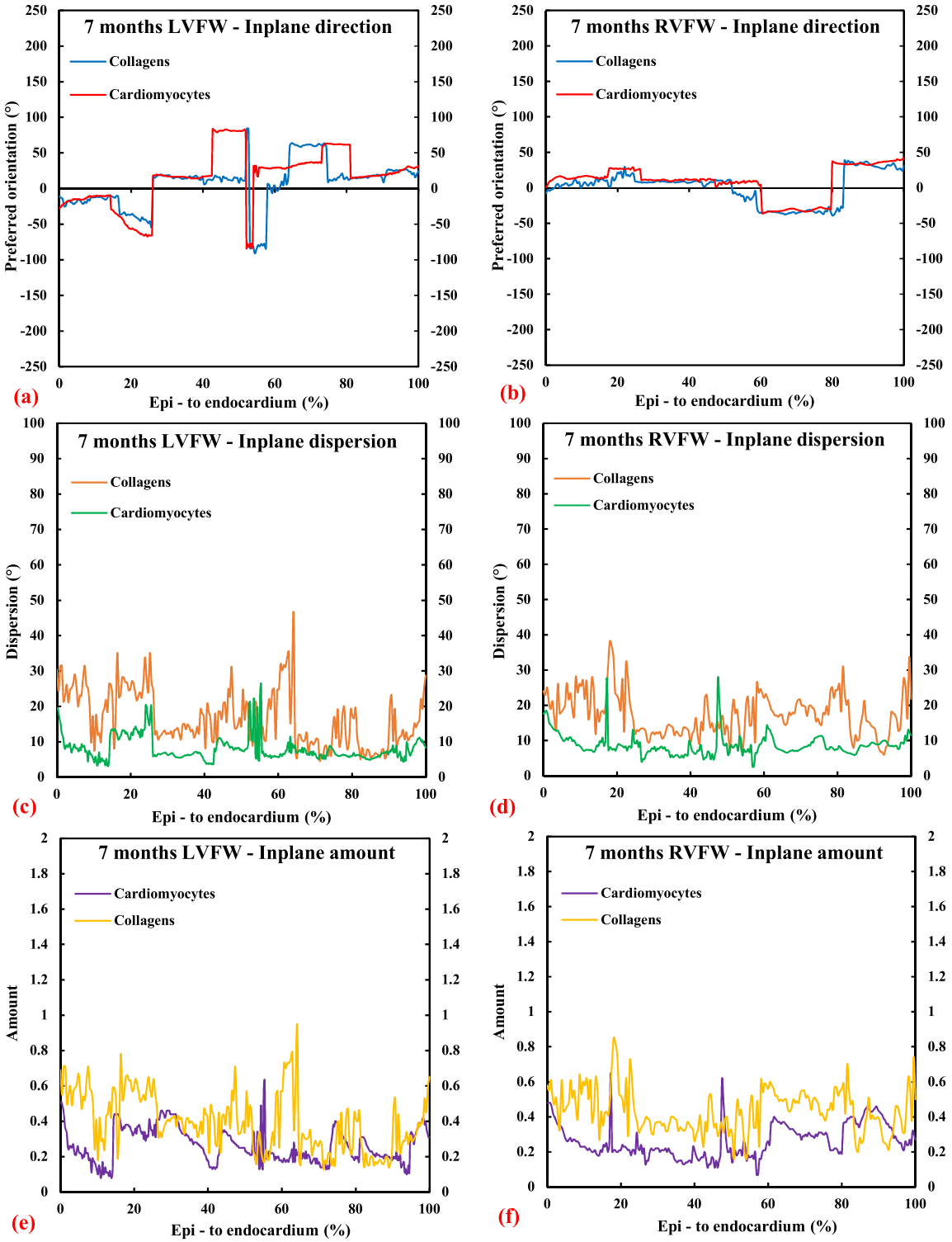

Fig. 5. TPEF/SHG microscopy was used to quantify the cardiomyocyte and collagen fibril microstructural parameters in the LVFW and RVFW ($n = 5$), consisting of in-plane preferred orientation, dispersion, and amount respectively. Microstructural data of two age groups are presented in this figure, namely, 7 months and 3 years old porcine hearts. ***7 months:*** (a) in-plane preferred orientation of 7 months LVFW; (b) in-plane preferred orientation of 7 months RVFW; (c) in-plane dispersion of 7 months LVFW; (d) in-plane dispersion of 7 months RVFW; (e) in-plane amount of 7 months LVFW; (f) in-plane amount of 7 months RVFW. ***3 years:*** (g) in-plane preferred orientation of 3 years LVFW; (h) in-plane preferred orientation of 3 years RVFW; (i) in-plane dispersion of 3 years LVFW; (j) in-plane dispersion of 3 years RVFW; (k) in-plane amount of 3 years LVFW; (l) in-plane amount of 3 years RVFW. In-plane image stacks were acquired through the absolute thickness of the LVFW and RVFW (i.e., epicardium to endocardium).

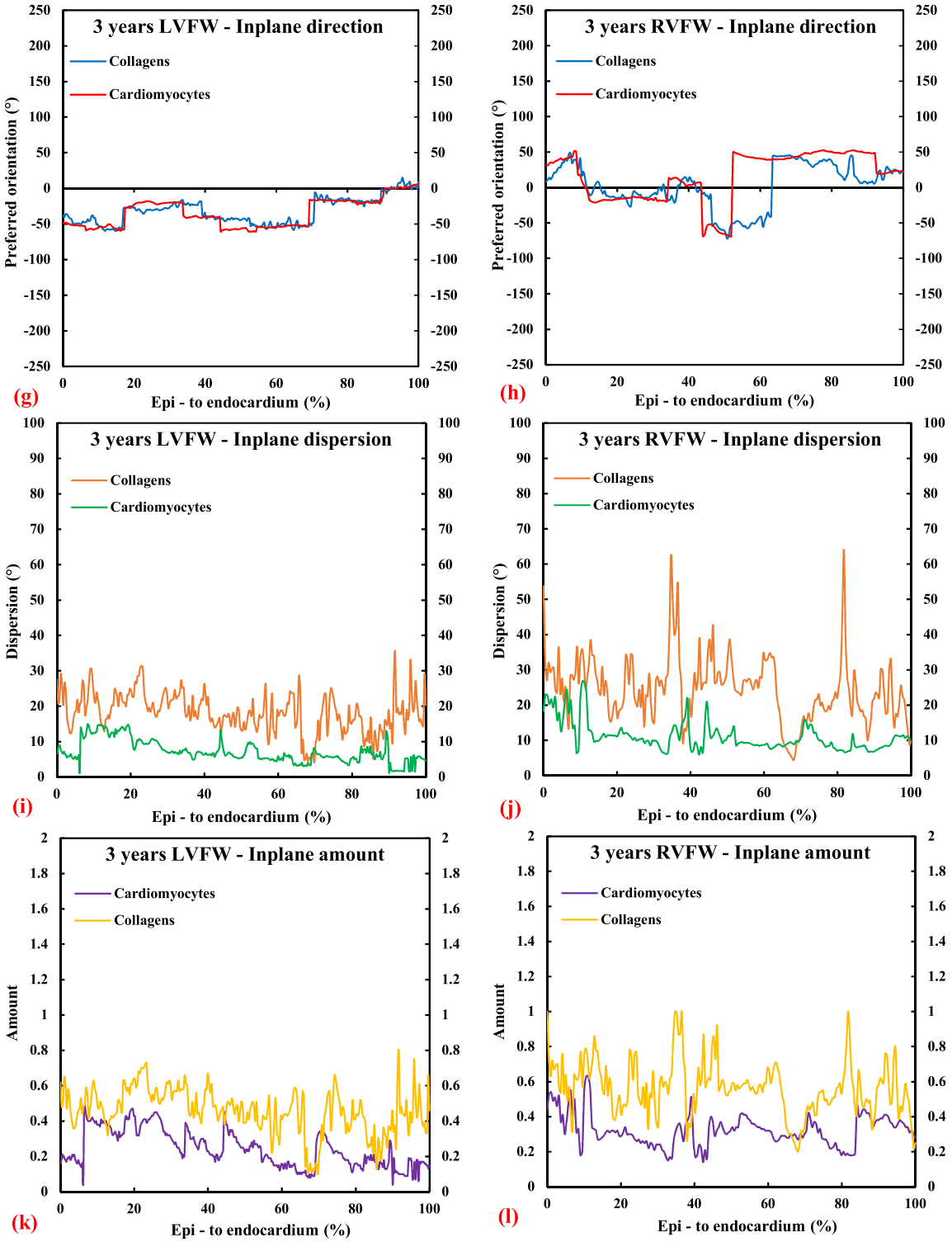

Fig. 5. Continued

Five preconditioning cycles were performed, starting at 2.5–15 % stretch, with an incremental increase of 2.5 %. The 1st and 5th cycles of 12.5 % and 15 % stretch levels are shown in Fig. 6 (a–h). The curves typically stabilised after three or four preconditioning cycles; hence, the 5th cycle was considered to represent actual behaviour, balancing achieving stability with minimising tissue damage. The average hysteresis area is a measure of energy dissipation. Table 3 shows the energy dissipation for MFD and CFD during equibiaxial testing at 10 % stretch. It was noted that the MFD exhibited greater energy dissipation than CFD up to 7 months, switching for the oldest tissue (Table 3). Energy dissipation was greater in the LVFW than in RVFW for both MFD and CFD (Table 3). Softening during the first preconditioning cycle was observed between subsequent stretch levels at all age groups (Fig. 6 (a–h).

The equi-biaxial behaviour of LVFW and RVFW at 10 % stretch is presented in Fig. 7 (a–h), with Cauchy stress increasing with age in

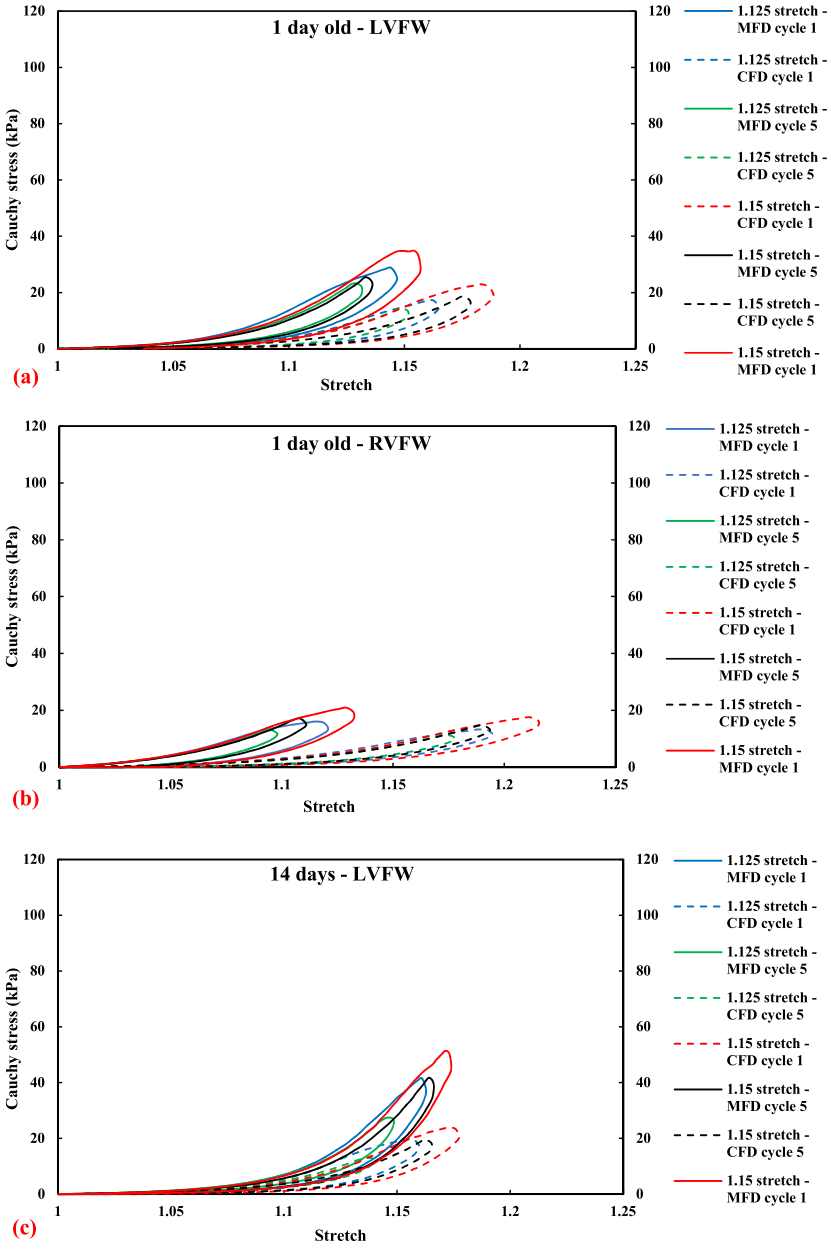

Fig. 6. Average preconditioning behaviour (Cauchy stress vs stretch) in the MFD (solid curves) and CFD (dashed curves) of porcine LVFW and RVFW specimens. Graphs representing typical preconditioned equibiaxial properties at subsequently increased stretch levels ranging from 1.125 to 1.15 in 0.025 increments. Representative preconditioning behaviour in terms of first and fifth loading-unloading cycles at two subsequent stretch levels (12.5 % and 15 %). Four age groups are presented in these graphs, namely 1-day-old LVFW (a) and RVFW(b); 14 days old LVFW (c) and RVFW (d); 7 months old LVFW (e) and RVFW (f); 3 years old LVFW (g) and RVFW (h).

Table 3
Average hysteresis area (energy dissipation per unit volume) of the porcine left and right ventricular free walls ($n = 40$) during equibiaxial testing (1:1) in the MFD and CFD. Average values for each age group are presented in Joule per cubic metre, representing the area between the loading and unloading stress–stretch curves.

Age-groups	Hysteresis area			
	MFD		CFD	
	LVFW J/m^3	RVFW J/m^3	LVFW J/m^3	RVFW J/m^3
1 day	771	647	664	608
14 days	824	777	595	530
7 months	2038	1096	997	291
3 years	953	742	1477	1021

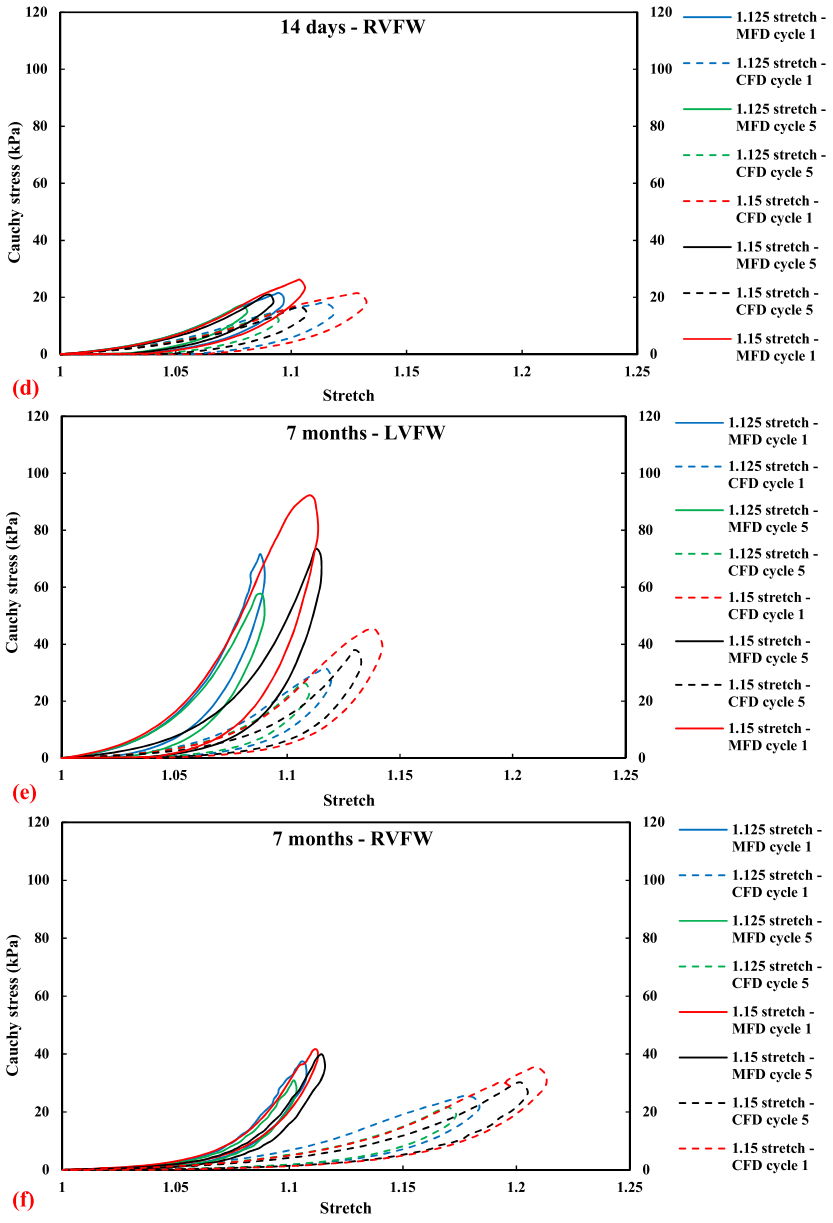

Fig. 6. Continued

both the MFD and CFD. Non-equibiaxial testing enabled evaluation of how the cross-coupling influenced stress in the MFD and CFD (Figs. 8 and 9 (a–p)), with either the MFD or CFD, possessing a relatively low stretch exhibiting a stiffer biomechanical response. The older tissue had a greater influence on cross-coupling, evidenced by the relatively high Cauchy stresses (Fig. 9 (a–h)). LVFW and RVFW tissue stiffness increase with age in both the MFD and CFD (Fig. 10a–c); however, in the RVFW, MFD stiffness only markedly increased at greater CFD stretch. In comparison, RVFW exhibited greater stiffness in the MFD across all age groups (Fig. 10e). Considering the CFD, the LVFW is the stiffest across all age groups (Fig. 10f). Measures are presented that enable tracking of biomechanical changes with G & R. The maximum and minimum tangent moduli were generated by the oldest and youngest tissue, respectively (Tables 4 and 5). The changes in tissue extensibility and the degree of anisotropy were noted with increasing age. The former decreased whilst the degree of anisotropy increased between 1 day and 3 years in MFD and CFD, with respect to age (Tables 4 and 5). A significant positive correlation ($p < 0.001$) was noted between the increasing tangent moduli and age (Table 6). Additional statistics are presented for the LVFW and RVFW in the MFD and CFD (Tables 7 and 8) and between LVFW and RVFW in the MFD and CFD (Table 9).

Viscoelasticity increased in the LVFW with age, especially between 7 months and 3 years in MFD and CFD as shown in (Fig. 11 a and b). Viscoelasticity in the RVFW also increased with age, though the CFD demonstrated a more gradual increase than MFD (Fig. 11 c and d). In comparison, RVFW was found to have a greater viscous behaviour than LVFW in the MFD and CFD, (Fig. 11 e and f).

4. Discussion

The LVFW and RVFW myocardial tissues exhibited non-linear, anisotropic, and viscoelastic biomechanical behaviour that varied with age (Figs. 7–9). The MFD is stiffer than CFD (Fig. 7). These overall traits are consistent with those reported in passive myocardial and other biological tissue studies [32,33,35,38,39]. Contrary to the passive stress anisotropy in the MFD and CFD, the active

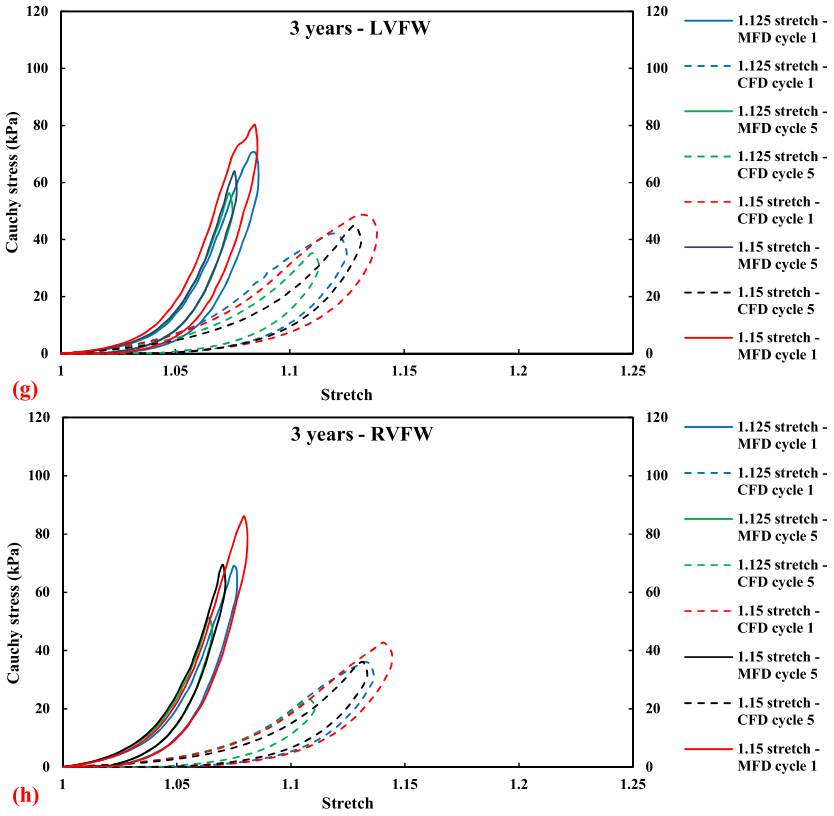

Fig. 6. Continued

Table 4
Mean and standard error values of biaxially determined biomechanical measurements for the left ventricle free wall (LVFW) at each age group.

LVFW	1 day	14 days	7 months	3 years
TM_{MFD}_low (kPa)	19 ± 8	75 ± 6	83 ± 7	93 ± 5
TM_{MFD}_high (kPa)	254 ± 10	270 ± 14	341 ± 19	788 ± 21
TM_{CFD}_low (kPa)	13 ± 3	33 ± 4	50 ± 9	87 ± 13
TM_{CFD}_high (kPa)	106 ± 12	130 ± 11	292 ± 15	345 ± 18
EXT_MFD	0.10 ± 0.02	0.05 ± 0.01	0.08 ± 0.02	0.05 ± 0.01
EXT_CFD	0.12 ± 0.03	0.07 ± 0.01	0.09 ± 0.02	0.08 ± 0.01
DA	0.94 ± 0.03	0.90 ± 0.03	0.86 ± 0.02	0.58 ± 0.02

TM_{MFD}_low – Tangent Modulus in the low, pretransitional region along the mean-fibre direction; TM_{MFD}_high – Tangent Modulus in the high, post-transitional region along the mean-fibre direction; TM_{CFD}_low – Tangent Modulus in the low, pretransitional region along the cross-fibre direction; TM_{CFD}_high – Tangent Modulus in the high, post-transitional region along the cross-fibre direction; EXT_MFD – Extensibility along the mean-fibre direction; EXT_CFD – Extensibility along the cross-fibre direction; DA – Degree of Anisotropy.

Table 5
Mean and standard error values of biaxially determined biomechanical measurements for the right ventricle free wall (RVFW) at each age group.

RVFW	1 day	14 days	7 months	3 years
TM_{MFD}_low (kPa)	62 ± 8	86 ± 9	103 ± 11	180 ± 16
TM_{MFD}_high (kPa)	157 ± 18	233 ± 23	651 ± 30	971 ± 39
TM_{CFD}_low (kPa)	16 ± 3	20 ± 2	27 ± 4	51 ± 7
TM_{CFD}_high (kPa)	76 ± 9	120 ± 15	147 ± 17	270 ± 24
EXT_MFD	0.05 ± 0.01	0.05 ± 0.01	0.08 ± 0.02	0.04 ± 0.01
EXT_CFD	0.11 ± 0.02	0.12 ± 0.01	0.16 ± 0.03	0.09 ± 0.01
DA	0.56 ± 0.03	0.55 ± 0.04	0.53 ± 0.03	0.51 ± 0.02

TM_{MFD}_low – Tangent Modulus in the low, pretransitional region along the mean-fibre direction; TM_{MFD}_high – Tangent Modulus in the high, post-transitional region along the mean-fibre direction; TM_{CFD}_low – Tangent Modulus in the low, pretransitional region along the cross-fibre direction; TM_{CFD}_high – Tangent Modulus in the high, post-transitional region along the cross-fibre direction; EXT_MFD – Extensibility along the mean-fibre direction; EXT_CFD – Extensibility along the cross-fibre direction; DA – Degree of Anisotropy.

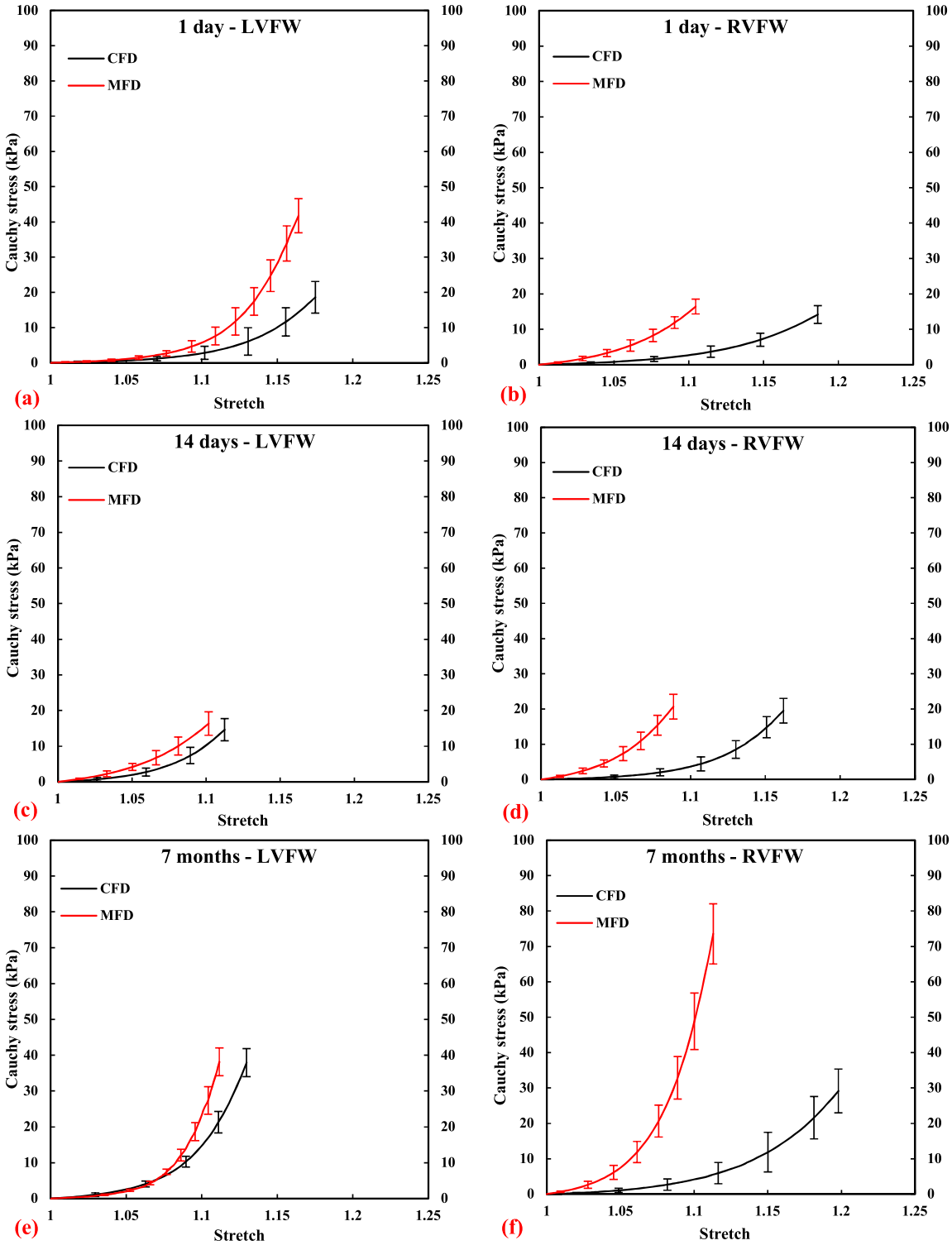

Fig. 7. Average 'elastic' equibiaxial (Cauchy stress vs. stretch) behaviour of all considered porcine LVFW (n = 40) and RVFW (n = 40) myocardial specimens subjected to a stretch of (1:1) in the MFD and CFD. Four age groups are presented in these graphs, namely 1-day-old LVFW (a) and RVFW(b); 14 days old LVFW (c) and RVFW (d); 7 months old LVFW (e) and RVFW (f); 3 years old LVFW (g) and RVFW (h). All data is presented in mean curves and corresponding standard errors indicated by error bars.

contraction study reported significantly greater stress in the CFD [40]. This behaviour is associated with the variations in contractility across the transmural depth in human and porcine hearts, where higher active forces in the endocardial and epicardial regions, compared to the mid-wall regions, may in part contribute to greater active stress in the CFD [40,72–75]. The Anisotropy in the MFD and CFD is mainly due to its intracellular fibrous protein, titin. Titin is a large elastic protein that connects the z-line of the sarcomere to the m-line. It primarily provides stiffness along the length of the sarcomere, causing anisotropy in the myocardial tissue (Fig. 7). The stiffness of the titin molecule prevents overextension of the sarcomere, to prevent any damage to the cells. The change in the degree of anisotropy (DA) was observed across four age groups (Tables 4 and 5), which may be due to the altered col-

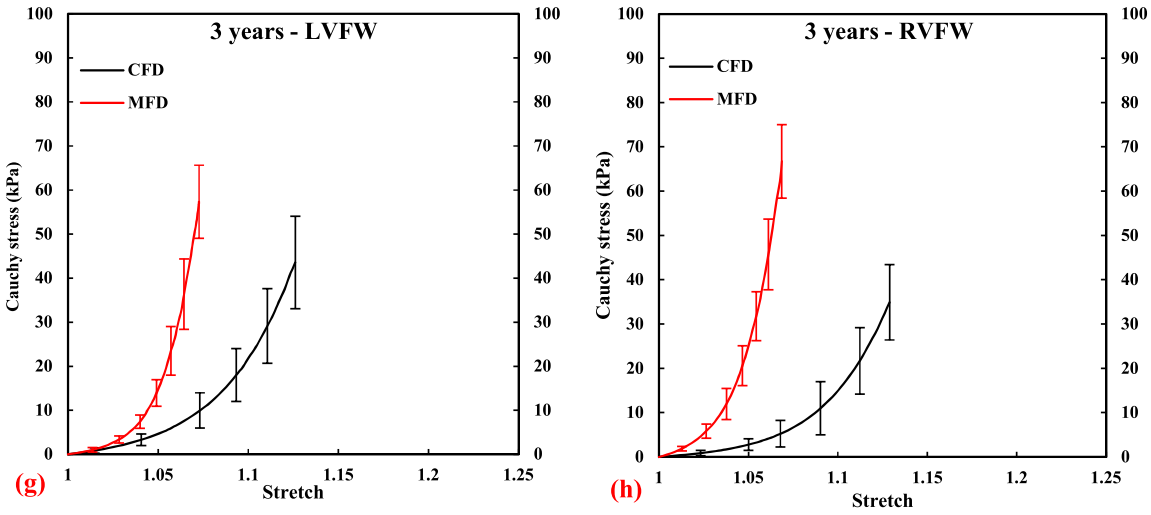

Fig. 7. Continued

Table 6
Correlation between biaxially determined material parameters and age groups (1 day, 14 days, 7 months, and 3 years) for the left ventricle-free wall (LVFW) and right ventricle-free wall (RVFW) of the porcine heart.

Heart regions		TM_{MFD}_low	TM_{MFD}_high	TM_{CFD}_low	TM_{CFD}_high	EXT_MFD	EXT_CFD	DA
LVFW	r	1	1	1	1	−0.6	−0.4	−1
	p	**<0.01**	**<0.01**	**<0.01**	**<0.01**	0.3	0.6	**<0.01**
RVFW	r	1	1	1	1	0.2	−0.2	−1
	p	**<0.01**	**<0.01**	**<0.01**	**<0.01**	0.7	0.8	**<0.01**

Bold-statistical significance using Spearman correlation.

Table 7
Statistical analysis (one-way ANOVA along with Tukey HSD post hoc test) of biaxial data for ***LVFW*** across four age groups, namely, 1 day, 14 days, 7 months, and 3 years old represent **(1)** LVFW (1 day and 14 days old) for MFD–CFD; **(2)** LVFW (1 day and 7 months old) for MFD–CFD; **(3)** LVFW (1 day and 3 years old) for MFD–CFD; **(4)** LVFW (14 days and 7 months old) for MFD–CFD; **(5)** LVFW (14 days and 3 years old) for MFD–CFD; and **(6)** LVFW (7 months and 3 years old) for MFD–CFD respectively. A p-value less than 0.05 is considered statistically significant.

LVFW	1 day		14 days		7 months		3 years	
Configurations	MFD	CFD	MFD	CFD	MFD	CFD	MFD	CFD
1 day and 14 days old	0.01	0.01	0.01	0.01	–	–	–	–
1 day and 7 months old	0.01	0.01	–	–	0.01	0.01	–	–
1 day and 3 years old	0.01	0.01	–	–	–	–	0.01	0.01
14 days and 7 months old	–	–	0.01	0.01	0.01	0.01	–	–
14 days and 3 years old	–	–	0.01	0.01	–	–	0.01	0.01
7 months and 3 years old	–	–	–	–	0.01	0.01	0.01	0.01

Table 8
Statistical analysis (one-way ANOVA along with Tukey HSD post hoc test) of biaxial data for ***RVFW*** across four age groups, namely, 1 day, 14 days, 7 months, and 3 years old represent **(1)** RVFW (1 day and 14 days old) for MFD–CFD; **(2)** RVFW (1 day and 7 months old) for MFD–CFD; **(3)** RVFW (1 day and 3 years old) for MFD–CFD; **(4)** RVFW (14 days and 7 months old) for MFD–CFD; **(5)** RVFW (14 days and 3 years old) for MFD–CFD; and **(6)** RVFW (7 months and 3 years old) for MFD–CFD respectively. A *p*-value less than 0.05 is considered statistically significant.

RVFW	1 day		14 days		7 months		3 years	
Configurations	MFD	CFD	MFD	CFD	MFD	CFD	MFD	CFD
1 day and 14 days old	0.01	0.01	0.01	0.01	–	–	–	–
1 day and 7 months old	0.01	0.01	–	–	0.01	0.01	–	–
1 day and 3 years old	0.01	0.01	–	–	–	–	0.01	0.01
14 days and 7 months old	–	–	0.01	0.01	0.01	0.01	–	–
14 days and 3 years old	–	–	0.01	0.06	–	–	0.01	0.06
7 months and 3 years old	–	–	–	–	0.01	0.01	0.01	0.01

lagen fibril alignment during G & R, as a result of the increased mechanical stress and strain within the myocardial tissue [22]. The RVFW exhibited greater anisotropy than the LVFW, which may be due to differences in their underlying microstructure, which significantly contributes to facilitating anatomical deformation mechanics during diastolic and systolic functions of the heart. This attribute is consistent with ovine heart tissue [42]. The LVFW and RVFW possessed relatively pronounced hysteresis, which identified a significant energy dissipation during biaxial tensile loading modes (Fig. 6). The MFD possessed greater energy dissipation than CFD in younger myocardial tissue (1 day, 14 days, and 7 months old) as depicted in Table 3. Greater energy dissipation was noted in the CFD for adult heart tissue (3 years old) (Table 1). This may be in part because of the G & R in the adulthood phase, causing the changes in the cardiac matrix [12,13]. In comparison, LVFW demonstrated greater energy dissipation than the RVFW, across four age groups (Table 3).

Softening was evident during the biaxial cyclic preconditioning, as shown in Fig. 6. The greatest change in stress was observed during the first two preconditioning cycles. This stress-softening

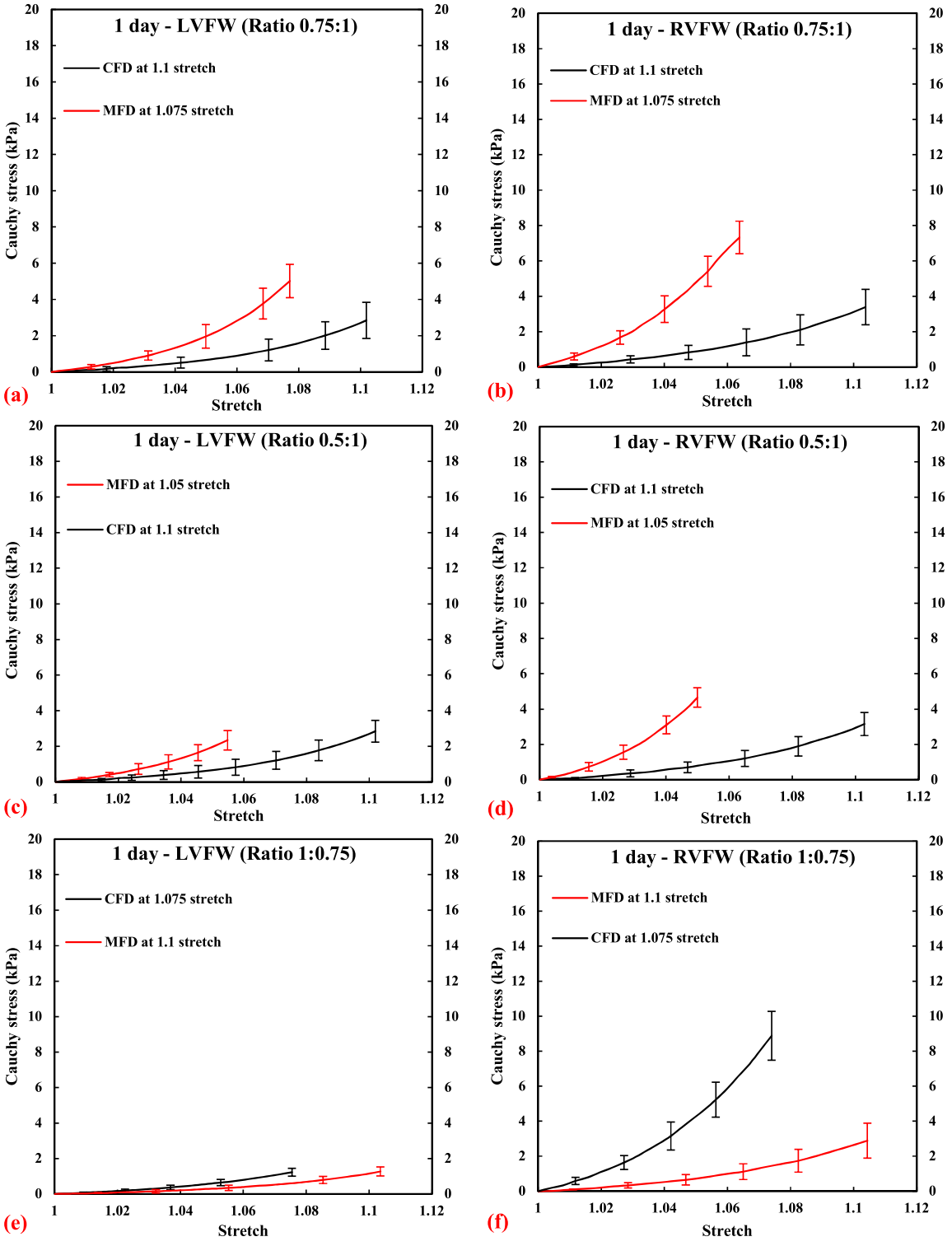

Fig. 8. Average non-equibiaxial (Cauchy stress vs. stretch) behaviour of all considered porcine LVFW (n = 20) and RVFW (n = 20) myocardial specimens subjected to non-equibiaxial stretch ratios, including 0.75:1; 0.5:1, 1:0.75, and 1:0.5 in the MFD and CFD, respectively. The red and black curves correspond to the mean fibre direction (MFD) and the cross-fibre direction (CFD). Two age groups are presented in these graphs, namely ***1-day-old***: LVFW at stretch ratio 0.75:1 (a), RVFW at stretch ratio 0.75:1 (b), LVFW at stretch ratio 0.5:1 (c), RVFW at stretch ratio 0.5:1 (d), LVFW at stretch ratio 1:0.75 (e), RVFW at stretch ratio 1:0.75 (f), LVFW at stretch ratio 1:0.5 (g), and RVFW at a stretch ratio 1:0.5 (h); ***14 days old***: LVFW at stretch ratio 0.75:1 (i), RVFW at stretch ratio 0.75:1 (j), LVFW at stretch ratio 0.5:1 (k), RVFW at stretch ratio 0.5:1 (l), LVFW at stretch ratio 1:0.75 (m), RVFW at stretch ratio 1:0.75 (n), LVFW at stretch ratio 1:0.5 (o), and RVFW at stretch ratio 1:0.5 (p). All data is presented in mean curves and corresponding standard errors indicated by error bars. (For interpretation of the references to colour in this figure legend, the reader is referred to the web version of this article.).

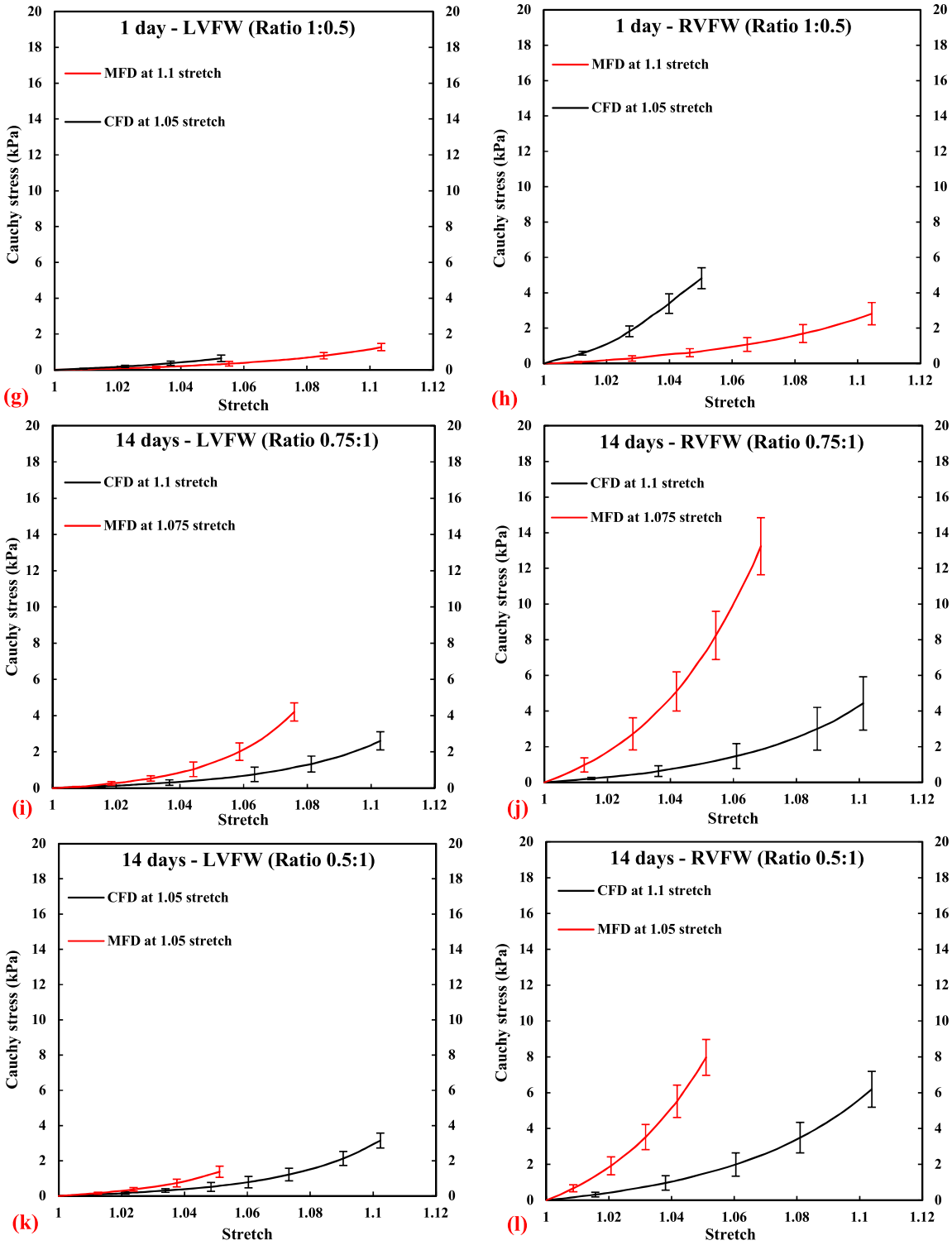

Fig. 8. Continued

behaviour is also referred to as the Mullins effect [76]. The pronounced strain softening was caused by the disruption of the perimysial collagen network, which is a consequence of the excessive shearing between adjacent myocardial muscle layers [77]. Moreover, strain softening may occur due to changes in the collagen matrix where the cardiomyocytes are embedded [78]. The relative increase in stiffness of the LVFW and RVFW myocardial tissues was noted from neonate to adulthood in the MFD and CFD (Fig. 10 and Tables 4 and 5). This is primarily due to the G & R producing new and renewing existing ECM, because of the increased ventricular workload [12,13,79]. Also, the relative increase in collagen fibril crosslinking and assembly, may in part contribute to increased stiffness of myocardial tissue, during G & R [11]. This provides high tensile strength (i.e., stiffness) to the tissue in response to the increased physiological demands [80,81]. Such changes in the composition, organisation and assembly of the new ECM ma-

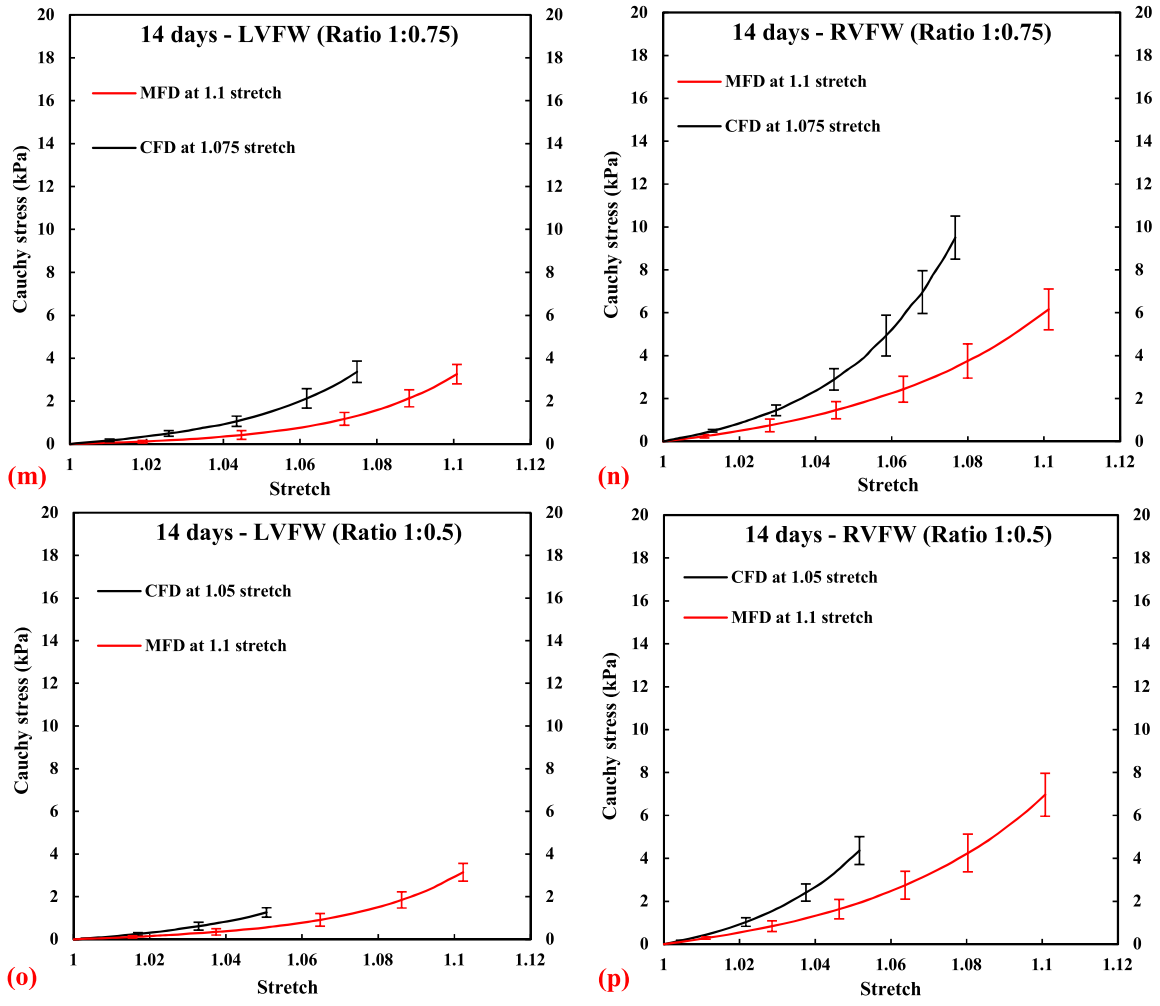

Fig. 8. Continued

Table 9
Statistical analysis (one-way ANOVA along with Tukey HSD post hoc test) of biaxial data for LVFW and RVFW across four age groups, namely, 1 day, 14 days, 7 months, and 3 years old in the MFD–CFD. A *p*-value less than 0.05 is considered statistically significant.

	LVFW		RVFW	
Age groups	MFD	CFD	MFD	CFD
1 day	0.01	0.07	0.01	0.07
14 days	0.01	0.01	0.01	0.01
7 months	0.01	0.01	0.01	0.01
3 years	0.01	0.01	0.01	0.01

terial have been reported to increase the biomechanical stiffness of the ventricle tissues during G & R [15,16]. This is consistent with the other biological tissue studies, reporting the effects of G & R on the overall biomechanical stiffness [44–49]. The RVFW myocardial tissue is stiffer than LVFW across all age groups in the MFD during biaxial tests (Fig. 10 and Tables 4 and 5). The relative variations in the left and right ventricles' biomechanical stiffness may be due to the difference in ventricular blood filling (diastole) and ejection (systole) during the cardiac cycle, as suggested in previous cardiac biaxial studies [15,37]. Conversely, right ventricular tissue has been reported as being less stiff than left in the MFD, during passive simple shear and uniaxial tensile/compression tests in ovine heart [43]. This may be due to the difference in deformation states, which correspond to the tissue's different contribution from its underlying microstructure (cardiomyocytes – interstitial collagen fibrils interaction) [43]. It also implies that G & R tends to happen at different rates in the LVFW and RVFW myocardial tissue, which may correspond to their mechanical constituents (stress, strain, strain energy density), maintaining the overall mechanical homoeostasis, during physiological ventricles development [3,82].

The viscoelasticity (Cauchy stress vs. time) appeared to increase from neonatal to adulthood, during G & R in both ventricles (Fig. 11). The RVFW myocardial tissue exhibited greater viscoelasticity than LVFW, across four age groups (Fig. 11). The myocardial tissue possesses a relatively high water content (~ 80 % wet weight) and is affected by muscle presence [83]. So, changes in water content may alter myocardium viscoelasticity during G & R [83]. The greater viscous behaviour in RVFW has also previously been reported in the ovine heart at high strains, which may in part contribute to preventing its structural integrity and physiological function [41]. The cardiomyocytes followed a consistent pattern in overall rotation and dispersion in LVFW and RVFW myocardial tissue (Figs. 3and 4 and Tables 1 and 2). It initially decreased in the early neonatal phase, followed by an increase in the mid-puberty phase, and finally decreased in the late adulthood phase. The early decrease may be due to an increase in the workload because of the rapid closing of the ductus arteriosus and foramen ovale, and reliance on pulmonary circulation [1,2]. The pronounced hypertrophy in both ventricles was observed in the mid-puberty

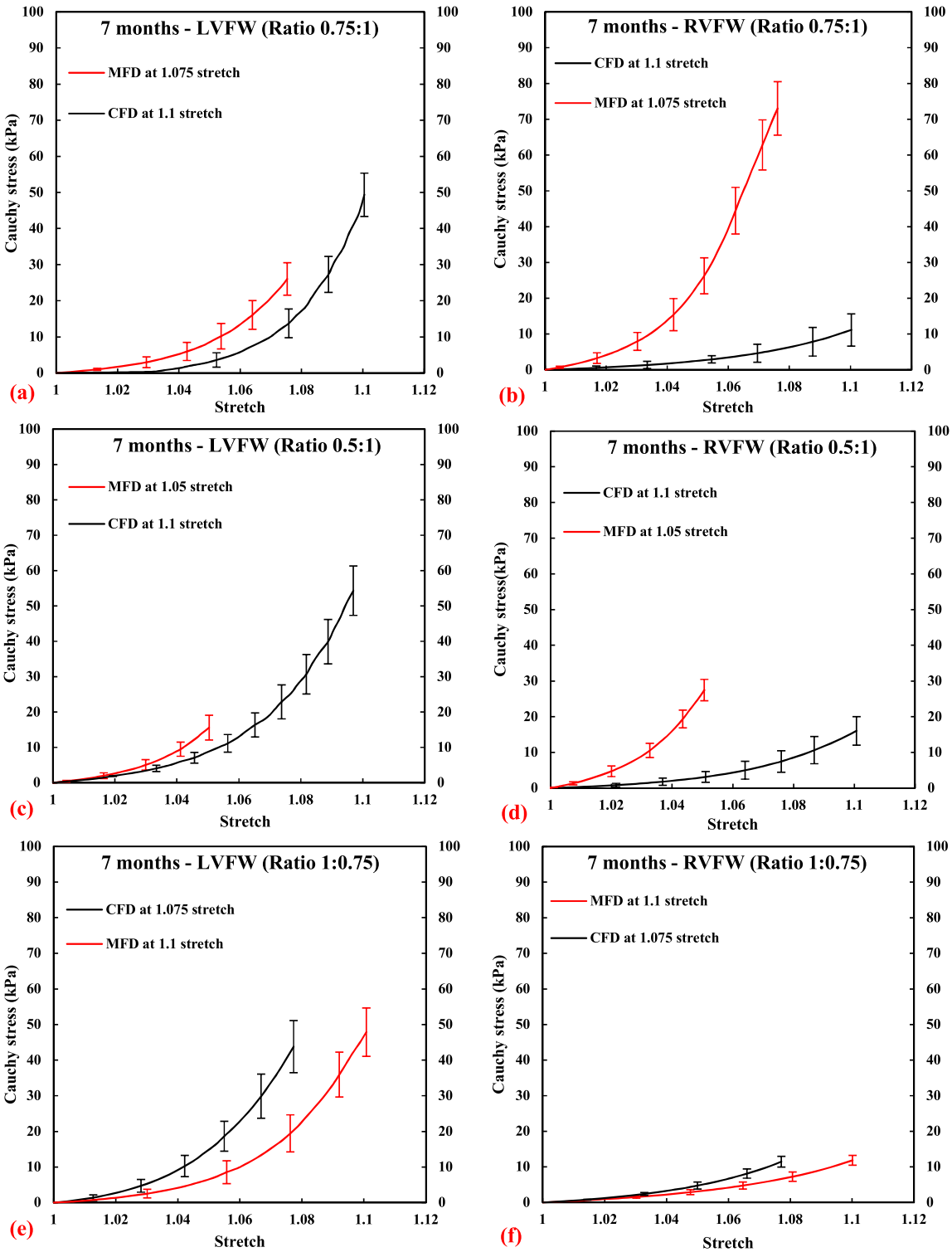

Fig. 9. Average non-equibiaxial (Cauchy stress vs. stretch) behaviour of all considered porcine LVFW (n = 20) and RVFW (n = 20) myocardial specimens subjected to non-equibiaxial stretch ratios, including 0.75:1; 0.5:1, 1:0.75, and 1:0.5 in the MFD and CFD, respectively. The red and black curves correspond to the mean fibre direction (MFD) and the cross-fibre direction (CFD). Two age groups are presented in these graphs, namely ***7 months old:*** LVFW at stretch ratio 0.75:1 (a), RVFW at stretch ratio 0.75:1 (b), LVFW at stretch ratio 0.5:1 (c), RVFW at stretch ratio 0.5:1 (d), LVFW at stretch ratio 1:0.75 (e), RVFW at stretch ratio 1:0.75 (f), LVFW at stretch ratio 1:0.5 (g), and RVFW at stretch ratio 1:0.5 (h); ***3 years old:*** LVFW at stretch ratio 0.75:1 (i), RVFW at stretch ratio 0.75:1 (j), LVFW at stretch ratio 0.5:1 (k), RVFW at stretch ratio 0.5:1 (l), LVFW at stretch ratio 1:0.75 (m), RVFW at stretch ratio 1:0.75 (n), LVFW at stretch ratio 1:0.5 (o), and RVFW at stretch ratio 1:0.5 (p). All data is presented in mean curves and corresponding standard errors indicated by error bars. (For interpretation of the references to colour in this figure legend, the reader is referred to the web version of this article.)

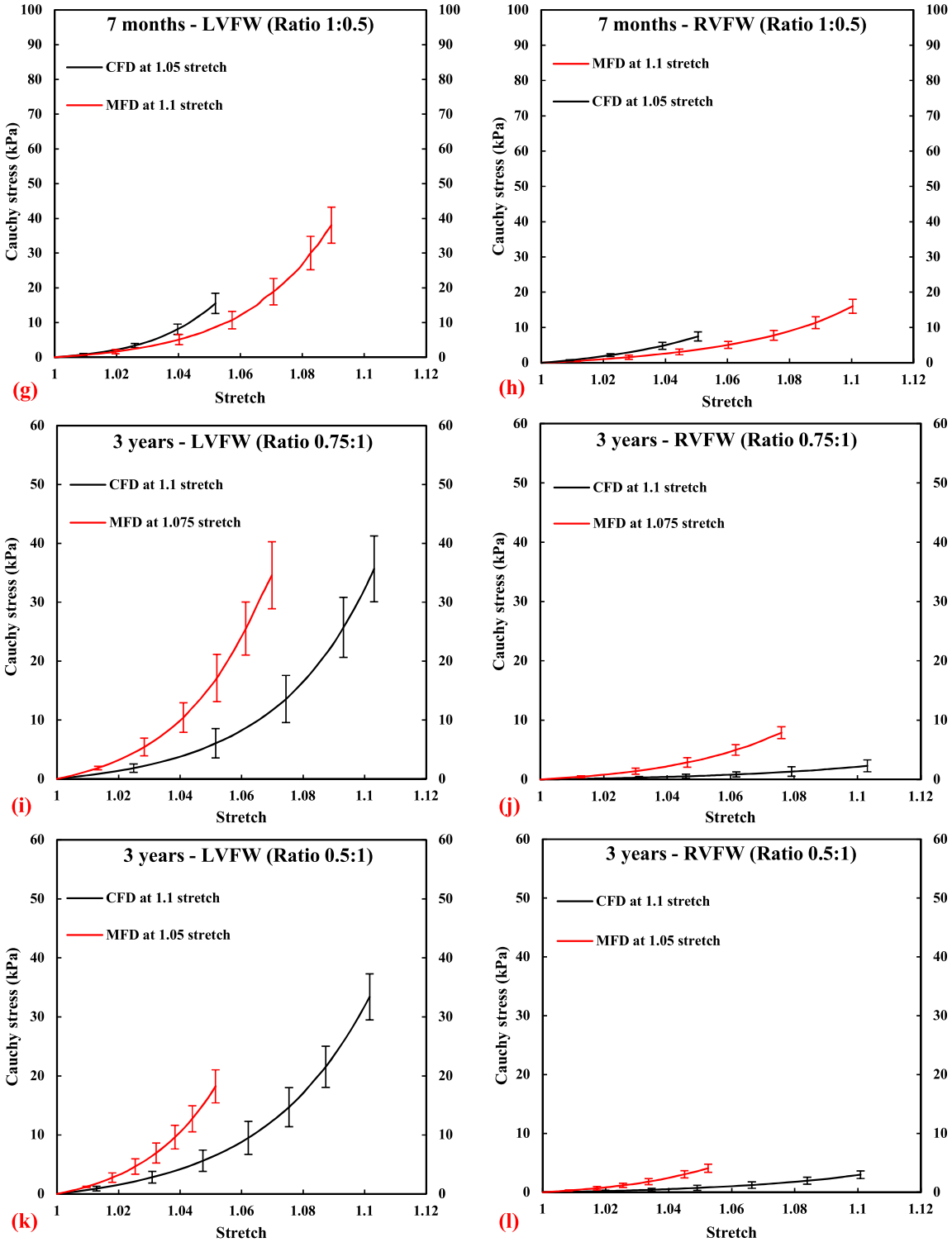

Fig. 9. Continued

phase, which may explain the relative increase in cardiomyocyte rotation and dispersion because of the rapidly increased volume (i.e., growth) in this phase (Fig. 1b and c). Whilst in the late adulthood phase, the decreased cardiomyocyte rotation and dispersion could in part be due to the change in ECM structure and composition, because of the G & R [12–14]. The adult LVFW (i.e., 3 years old ~ 250°) cardiomyocyte rotation reported here is similar to human and porcine heart studies, as reported in Table 1 [37,84]. Also, the total left ventricle cardiomyocyte rotation from epi–to-endocardium has been reported to be 140°in rats [85], 135° in guinea pigs [86], 140°in dogs [87], and 106° in mice [86]. Contrary to cardiomyocytes, collagen fibrils' rotation and dispersion continuously increased in both ventricles, across four age groups during G & R (Figs. 3 and 4 and Tables 1 and 2). This in-plane rotation and dispersion of interstitial collagen are important because they provide myocardium structural stability and organise the car-

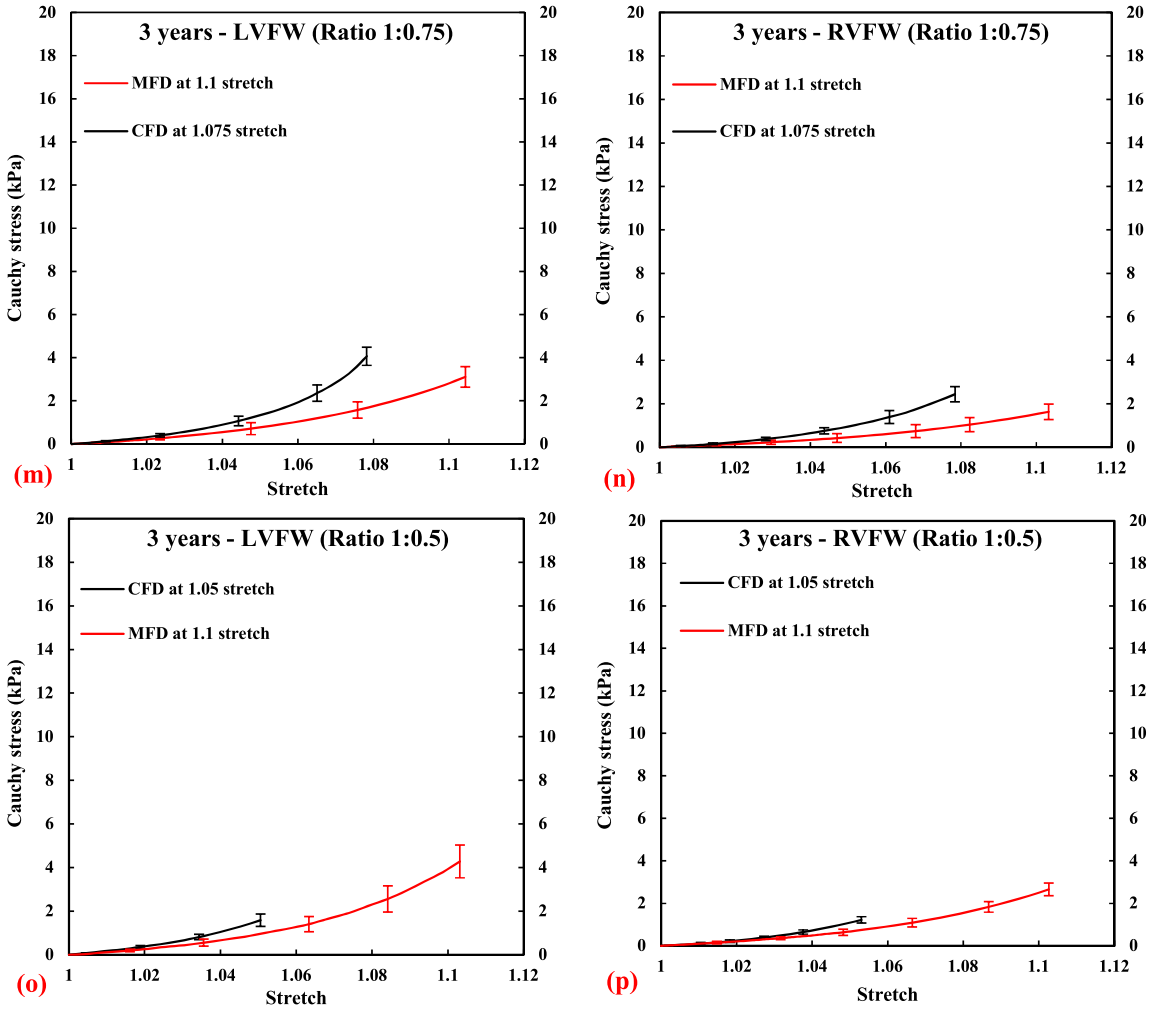

Fig. 9. Continued

diomyocytes' architecture in a higher order of laminar sheet layers [88,89]. Moreover, it is an essential framework for preserving the spatial registration of cardiomyocytes, such as limiting the extension of cardiomyocytes during diastole and transmitting the force and storage of energy during systole [85]. The interstitial collagens are cross-linked, and this provides high tensile strength, which significantly contributes to functionality during diastole [80,90]. This preserves the myocardium shape and wall thickness, and it also prevents ventricular aneurysms and rupture [91,92].

In this study, there is strong comparability between the peak equibiaxial Cauchy stress for the LVFW and RVFW, versus our previously published 1-day-old porcine heart data [93]. A comparison of our 3-year-old data versus adult human heart data shows porcine LVFW is 6-fold and 4-fold stiffer in the MFD and CFD, respectively [37]. Also, porcine RVFW is 4-fold and 2-fold stiffer in the MFD and CFD [37]. Quantitatively, a 3-fold increase in the stiffness (TM_{MFD}_high) was noted in the LVFW from neonatal to adulthood (Table 4), compared to a 6-fold increase in the RVFW (Table 5). In comparison, RVFW possessed 1.2-fold greater stiffness than LVFW (Tables 4 and 5). In both ventricles, the changes in extensibility (EXT) and degree of anisotropy (DA) in the MFD and CFD were observed. The former decreased whilst the anisotropy increased between neonatal to adulthood, during G & R (Tables 4 and 5). A 2-fold increase was reported in the LVFW cardiomyocyte rotation and dispersion between neonatal to adulthood (Table 1). This difference was almost negligible for the RVFW (Table 2). In contrast, collagen fibril rotation and dispersion continuously increased between neonatal to adulthood in the LVFW and RVFW (Tables 1 and 2). The former exhibited a 5-fold and 7-fold increase in rotation and dispersion (Table 1), whilst the RVFW had a 3-fold and 2-fold increase in rotation and dispersion (Table 2). Overall, LVFW demonstrated a greater degree of cardiomyocyte and collagen fibrils rotation and dispersion through the wall (i.e., epicardium to endocardium) (Tables 1 and 2). This may, in part contribute to the twisting of the left ventricle during systole and diastole, to determine the myocardial compliance and left ventricle suction, which in turn regulates the diastolic function of the heart [94,95].

4.1. Limitations

While these results provide valuable insight into the microstructural and biomechanical changes in the LVFW and RVFW myocardial tissue during G & R, it is acknowledged that an animal-based laboratory study differs from human, physiological reality. The porcine animal model was adopted as it is a widely accepted animal surrogate model for cardiac-related biomedical research and clinical trials. However, there are still differences that will limit the applicability of these data. While the controlled environment of a laboratory has significant advantages when investigating tissue characteristics, the need to dissect samples does create artificial boundary conditions and releases residual stresses, which may slightly alter the microstructural arrangement and could po-

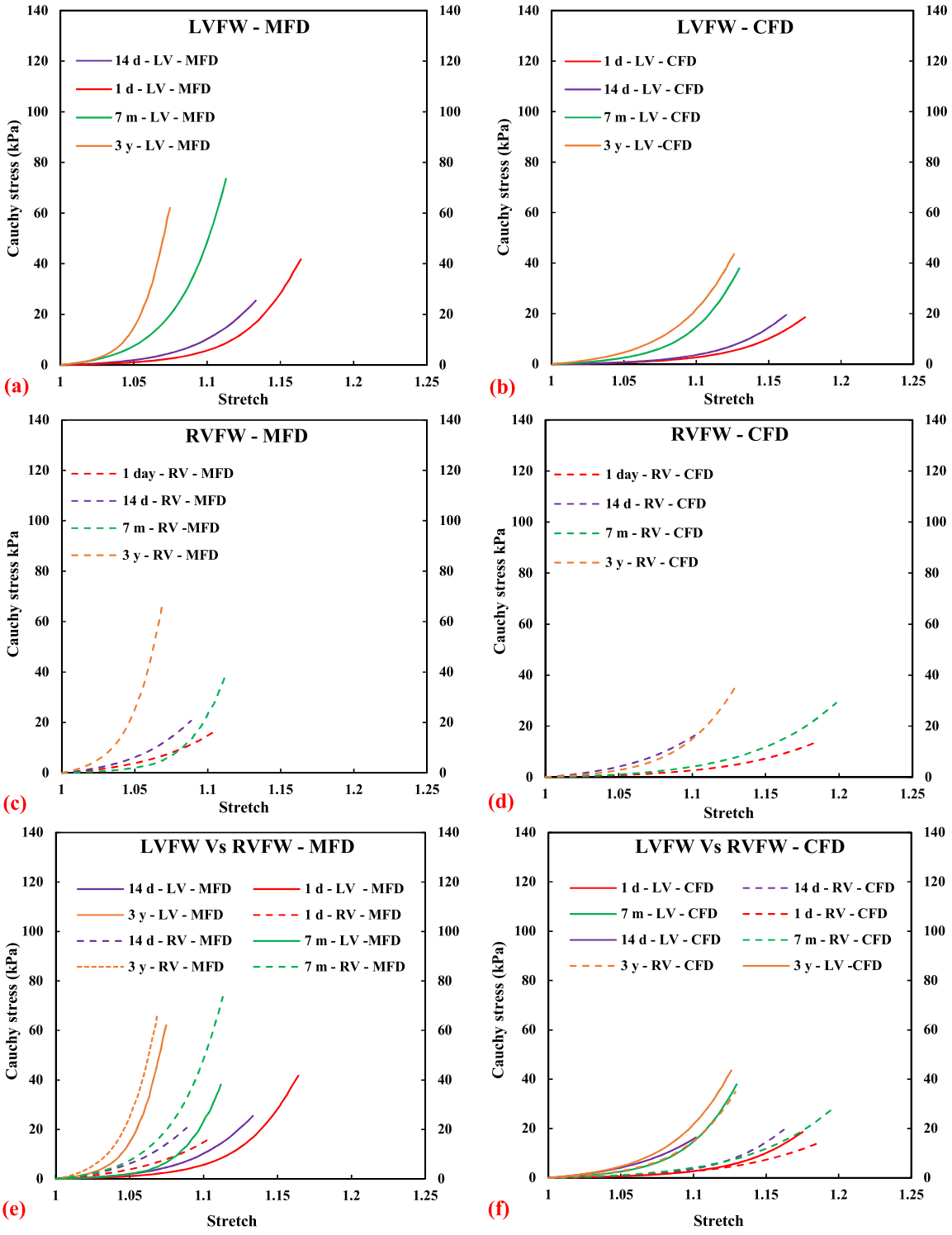

Fig. 10. Graphs representing the quantitative comparison of the mean equibiaxial behaviour (Cauchy stress vs stretch) of the porcine LVFW and RVFW myocardial specimens in the MFD and CFD across all four age groups (1-day, 14 days, 7 months, and 3 years old). LVFW in the MFD (a), LVFW in the CFD (b), RVFW in the MFD (c), RVFW in the CFD (d), LVFW vs RVFW in the MFD (e), and LVFW vs RVFW in the CFD (f). In this figure, LVFW and RVFW curves are presented in solid and dashed lines for easy interpretation.

tentially cause sharp changes in the cardiomyocytes and collagen fibrils direction and dispersion. Myocardium was considered incompressible for the simplicity of mathematical calculations in this study [37,96]. The deceased piglets were used to harvest the 1-day-old hearts for the biomechanical and microstructural analyses. These piglets were presumed to die because of hypoxia. Hence, it is unknown whether this route of death affects the tissue structure or mechanical behaviour. Common protocols were followed to ensure that the tissues remained hydrated, though there is no doubt that the deformations imposed by equibiaxial and non-equibiaxial testing differ from those experienced in typical cardiac physiology. The above-mentioned factors, plus the passiveness of the heart muscle, may also contribute to the strain softening observed in this study and may explain the softening behaviour observed at very

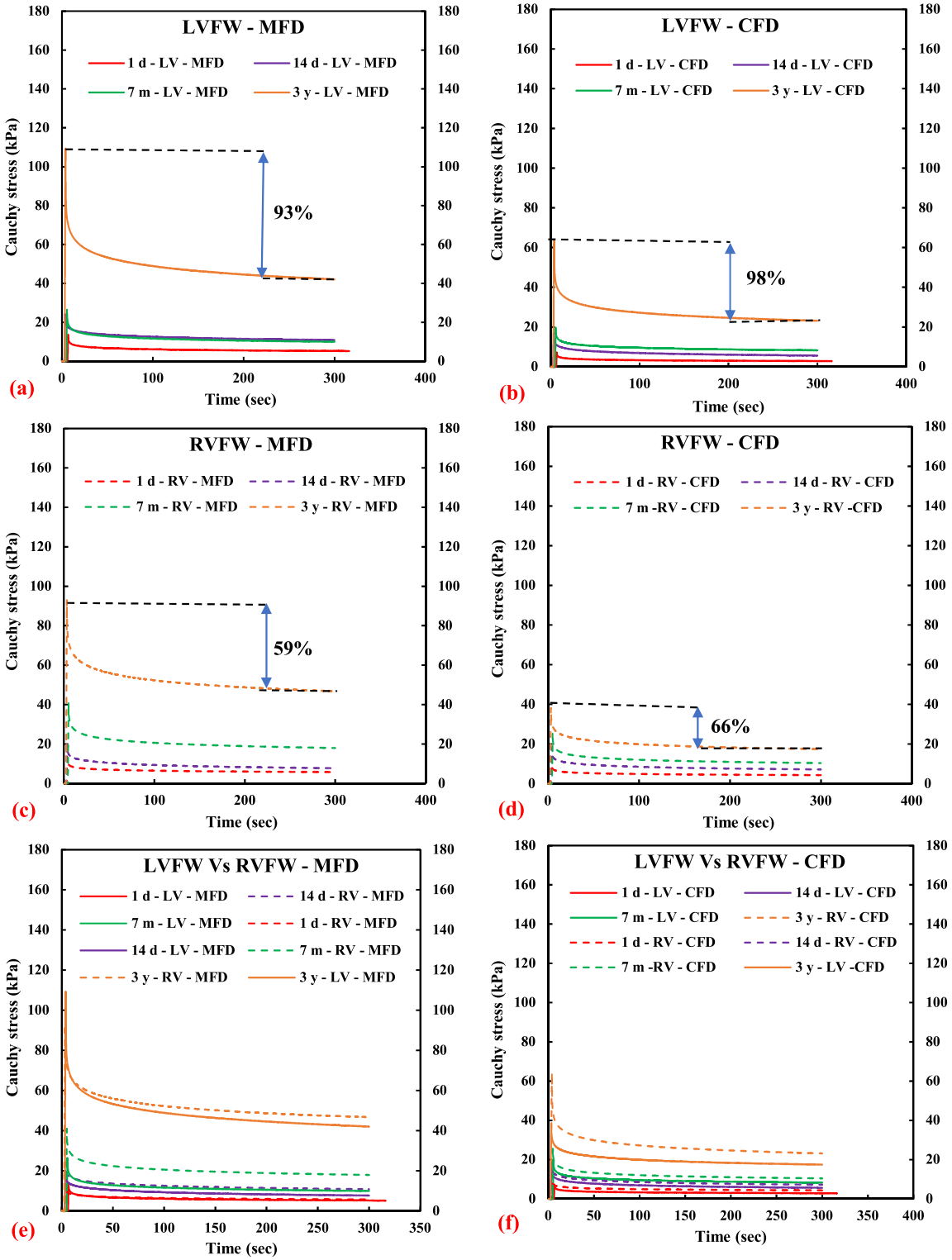

Fig. 11. Average stress relaxation (viscoelastic) behaviour of porcine LVFW (n = 20) and RVFW (n = 20) myocardial specimens at 10 % stretch during 5 min. All specimens were subjected to equibiaxial (1:1) stretch in the MFD and CFD respectively. Four age groups (1 day, 14 days, 7 months, and 3 years old) are presented for LVFW and RVFW in the MFD and CFD. LVFW in the MFD (a), LVFW in the CFD (b), RVFW in the MFD (c), RVFW in the CFD (d), LVFW vs RVFW in the MFD (e), and LVFW vs RVFW in the CFD (f). In this figure, LVFW and RVFW curves are presented in solid and dashed lines for easy interpretation. The percentage changes in the viscoelasticity of the LVFW and RVFW MFD and CFD were calculated for the older heart, to provide the baseline quantitative changes (a–d).

small strains. TPEF/SHG microscopy was used to evaluate the cardiomyocytes and collagen fibrils' orientation, dispersion, and concentration. The cause of getting greater collagen concentration is due to the Second harmonic generation (SHG) microscopy's superior signal generation ability to detect collagens than Two-photon excitation microscopy (TPEF) for cardiomyocytes. Specifically, SHG signals depend on the orientation, polarization, and local symmetry properties of chiral molecules, whereas TPEF results from the nonlinear excitation of molecular fluorescence. Whilst the issues associated with *in vitro* mechanical testing may limit the reliability of explicit material parameter identification, the approach used here has provided important, novel data on the G & R material response of the passive LVFW and RVFW myocardial tissue.

5. Conclusion

Ventricular tissue demonstrated non-linear, anisotropic, and viscoelastic behaviour, with stiffness and viscoelasticity increasing with G & R. Microstructural analyses revealed prominent changes in cardiomyocyte rotation and dispersion. Collagen fibrils rotation and dispersion continuously increased between neonatal to adulthood in both ventricles. This study provides baseline data that may prove useful to bioengineers, researchers, and mathematicians, to develop age-specific, G & R-based, constitutive models for enhanced computational simulations.

Declaration of Competing Interest

The authors declare that they have no known competing financial interests or personal relationships that could have appeared to influence the work reported in this paper.

Data availability

The complete dataset is accessible to other researchers at: http://doi.org/10.17035/d.2023.0272139483.

Acknowledgements

FA, SS and PT were supported by Engineering and Physical Sciences Research Council (EPSRC) funding (EP/S014195/1). The authors gratefully acknowledge the assistance of Rujing Lei and Lanxi Xu in data collection.

References

[1] N. Assali, N. Sehgal, S. Marable, Pulmonary and ductus arteriosus circulation in the fetal lamb before and after birth, Am. J. Physiol. Leg. Content 202 (3) (1962) 536–540.
[2] G. Dawes, J.C. Mott, J. Widdicombe, Closure of the foramen ovale in newborn lambs, J. Physiol. (Lond.) 128 (2) (1955) 384.
[3] D. Ambrosi, G.A. Ateshian, E.M. Arruda, S. Cowin, J. Dumais, A. Goriely, G.A. Holzapfel, J.D. Humphrey, R. Kemkemer, E. Kuhl, Perspectives on biological growth and remodeling, J. Mech. Phys. Solids 59 (4) (2011) 863–883.
[4] J.D. Humphrey, E.R. Dufresne, M.A. Schwartz, Mechanotransduction and extracellular matrix homeostasis, Nat. Rev. Mol. Cell Biol. 15 (12) (2014) 802–812.
[5] C.J. Beinlich, C.J. Rissinger, H.E. Morgan, Mechanisms of rapid growth in the neonatal pig heart, J. Mol. Cell. Cardiol. 27 (1) (1995) 273–281.
[6] W. Carver, L. Terracio, T.K. Borg, Expression and accumulation of interstitial collagen in the neonatal rat heart, Anat. Rec. 236 (3) (1993) 511–520.
[7] R.G. Cox, Smith's Anesthesia for Infants and Children, Springer, 2011.
[8] D.L. McAllister, L.D. Martin, D.O. Warner, A practice of anesthesia for infants and children, J. Am. Soc. Anesthesiol. 99 (4) (2003) 1035.
[9] C.R.G. Debessa, L.B.M. Maifrino, R.R. de Souza, Age related changes of the collagen network of the human heart, Mech. Ageing Dev. 122 (10) (2001) 1049–1058.
[10] C.T. Nguyen, C.S. Hall, M.J. Scott, Q. Zhu, J. Marsh, S.A. Wickline, Age-related alterations of cardiac tissue microstructure and material properties in Fischer 344 rats, Ultrasound Med. Biol. 27 (5) (2001) 611–619.
[11] M.L. Lindsey, D.K. Goshorn, C.E. Squires, G.P. Escobar, J.W. Hendrick, J.T. Mingoia, S.E. Sweterlitsch, F.G. Spinale, Age-dependent changes in myocardial matrix metalloproteinase/tissue inhibitor of metalloproteinase profiles and fibroblast function, Cardiovasc. Res. 66 (2) (2005) 410–419.
[12] P.J.A. Oomen, S. Loerakker, D. van Geemen, J. Neggers, M.T.H. Goumans, A.J. van den Bogaerdt, A. Bogers, C.V.C. Bouten, F.P.T. Baaijens, Age-dependent changes of stress and strain in the human heart valve and their relation with collagen remodeling, Acta Biomater. 29 (2016) 161–169.
[13] D. van Geemen, A.L. Soares, P.J. Oomen, A. Driessen-Mol, M.W. Janssen-van den Broek, A.J. van den Bogaerdt, A.J. Bogers, M.J. Goumans, F.P. Baaijens, C.V. Bouten, Age-dependent changes in geometry, tissue composition and mechanical properties of fetal to adult cryopreserved human heart valves, PLoS One 11 (2) (2016) e0149020.
[14] E. Aikawa, P. Whittaker, M. Farber, K. Mendelson, R.F. Padera, M. Aikawa, F.J. Schoen, Human semilunar cardiac valve remodeling by activated cells from fetus to adult: implications for postnatal adaptation, pathology, and tissue engineering, Circulation 113 (10) (2006) 1344–1352.
[15] F. Ahmad, R.J. Prabhu, J. Liao, S. Soe, M.D. Jones, J. Miller, P. Berthelson, D. Enge, K.M. Copeland, S. Shaabeth, R. Johnston, I. Maconochie, P.S. Theobald, Biomechanical properties and microstructure of neonatal porcine ventricles, J. Mech. Behav. Biomed. Mater. 88 (2018) 18–28.
[16] J.W. Holmes, J.A. Nuñez, J.W. Covell, Functional implications of myocardial scar structure, Am. J. Physiol. 272 (5 Pt 2) (1997) H2123–H2130.
[17] C.J. Coté, J. Lerman, I.D. Todres, A Practice of Anesthesia for Infants and Children E-book: Expert consult: Online and Print, Elsevier Health Sciences, 2012.
[18] R.G. Cox, Smith's anesthesia for infants and children, Can. J. Anesth./J. Can. Anesth. 58 (10) (2011) 973.
[19] L.A. Taber, S. Chabert, Theoretical and experimental study of growth and remodeling in the developing heart, Biomech. Model. Mechanobiol. 1 (1) (2002) 29–43.
[20] K. Tobita, J.B. Garrison, L.J. Liu, J.P. Tinney, B.B. Keller, Three-dimensional myofiber architecture of the embryonic left ventricle during normal development and altered mechanical loads, Anatom. Rec. Part A, Discov. Mol., Cell. Evol. Biol. 283 (1) (2005) 193–201.
[21] G.M. Fomovsky, A.D. Rouillard, J.W. Holmes, Regional mechanics determine collagen fiber structure in healing myocardial infarcts, J. Mol. Cell. Cardiol. 52 (5) (2012) 1083–1090.
[22] A.P. Voorhees, H.C. Han, Biomechanics of cardiac function, Compr. Physiol. 5 (4) (2015) 1623–1644.
[23] J. Humphrey, J. Eberth, W. Dye, R. Gleason, Fundamental role of axial stress in compensatory adaptations by arteries, J. Biomech. 42 (1) (2009) 1–8.
[24] S. Göktepe, O.J. Abilez, K.K. Parker, E. Kuhl, A multiscale model for eccentric and concentric cardiac growth through sarcomerogenesis, J. Theor. Biol. 265 (3) (2010) 433–442.
[25] C. Obbink-Huizer, C.W. Oomens, S. Loerakker, J. Foolen, C.V. Bouten, F.P. Baaijens, Computational model predicts cell orientation in response to a range of mechanical stimuli, Biomech. Model. Mechanobiol. 13 (1) (2014) 227–236.
[26] M.K. Rausch, F.A. Tibayan, D.C. Miller, E. Kuhl, Evidence of adaptive mitral leaflet growth, J. Mech. Behav. Biomed. Mater. 15 (2012) 208–217.
[27] C.J. Cyron, J.D. Humphrey, Vascular homeostasis and the concept of mechanobiological stability, Int. J. Eng. Sci. 85 (2014) 203–223.
[28] A. Vigliotti, W. Ronan, F.P. Baaijens, V.S. Deshpande, A thermodynamically motivated model for stress-fiber reorganization, Biomech. Model. Mechanobiol. 15 (4) (2016) 761–789.
[29] T.S. Eriksson, A.J. Prassl, G. Plank, G.A. Holzapfel, Influence of myocardial fiber/sheet orientations on left ventricular mechanical contraction, Math. Mech. Solids 18 (6) (2013) 592–606.
[30] G.A. Holzapfel, J.A. Niestrawska, R.W. Ogden, A.J. Reinisch, A.J. Schriefl, Modelling non-symmetric collagen fibre dispersion in arterial walls, J. R. Soc. Interface 12 (106) (2015) 20150188.
[31] L.L. Demer, F. Yin, Passive biaxial mechanical properties of isolated canine myocardium, J. Physiol. (Lond.) 339 (1) (1983) 615–630.
[32] M.R. Hill, M.A. Simon, D. Valdez-Jasso, W. Zhang, H.C. Champion, M.S. Sacks, Structural and mechanical adaptations of right ventricle free wall myocardium to pressure overload, Ann. Biomed. Eng. 42 (12) (2014) 2451–2465.
[33] J.D. Humphrey, R.K. Strumpf, F.C. Yin, Determination of a constitutive relation for passive myocardium: II. Parameter estimation, J. Biomech. Eng. 112 (3) (1990) 340–346.
[34] V.P. Novak, F.C. Yin, J.D. Humphrey, Regional mechanical properties of passive myocardium, J. Biomech. 27 (4) (1994) 403–412.
[35] M.S. Sacks, C.J. Chuong, Biaxial mechanical properties of passive right ventricular free wall myocardium, J. Biomech. Eng. 115 (2) (1993) 202–205.
[36] F.C. Yin, R.K. Strumpf, P.H. Chew, S.L. Zeger, Quantification of the mechanical properties of noncontracting canine myocardium under simultaneous biaxial loading, J. Biomech. 20 (6) (1987) 577–589.
[37] G. Sommer, A.J. Schriefl, M. Andrä, M. Sacherer, C. Viertler, H. Wolinski, G.A. Holzapfel, Biomechanical properties and microstructure of human ventricular myocardium, Acta Biomater. 24 (2015) 172–192.
[38] H. Ngwangwa, F. Nemavhola, T. Pandelani, M. Msibi, I. Mabuda, N. Davies, T. Franz, Determination of cross-directional and cross-wall variations of passive biaxial mechanical properties of rat myocardia, Processes 10 (4) (2022) 629.
[39] F. Nemavhola, Study of biaxial mechanical properties of the passive pig heart: material characterisation and categorisation of regional differences, Int. J. Mech. Mater. Eng. 16 (1) (2021) 6.
[40] S. Neelakantan, M. Kumar, E.A. Mendiola, H. Phelan, V. Serpooshan, S. Sadayappan, R. Avazmohammadi, Multiscale characterization of left ventricle active behavior in the mouse, Acta Biomater. 162 (2023) 240–253.

[41] W. Liu, M. Nguyen-Truong, M. Ahern, K.M. Labus, C.M. Puttlitz, Z. Wang, Different passive viscoelastic properties between the left and right ventricles in healthy adult ovine, J. Biomech. Eng. 143 (12) (2021) 121002–121011.
[42] W. Liu, M. Nguyen-Truong, K. LeBar, K.M. Labus, E. Gray, M. Ahern, S. Neelakantan, R. Avazmohammadi, K.C. McGilvray, C.M. Puttlitz, Z. Wang, Multiscale contrasts between the right and left ventricle biomechanics in healthy adult sheep and translational implications, Front. Bioeng. Biotechnol. 10 (2022) 857638.
[43] S. Kakaletsis, W.D. Meador, M. Mathur, G.P. Sugerman, T. Jazwiec, M. Malinowski, E. Lejeune, T.A. Timek, M.K. Rausch, Right ventricular myocardial mechanics: multi-modal deformation, microstructure, modeling, and comparison to the left ventricle, Acta Biomater. 123 (2021) 154–166.
[44] P. Chantereau, M. Brieu, M. Kammal, J. Farthmann, B. Gabriel, M. Cosson, Mechanical properties of pelvic soft tissue of young women and impact of aging, Int. Urogynecol. J. 25 (11) (2014) 1547–1553.
[45] B. Derby, R. Akhtar, Mechanical Properties of Aging Soft Tissues, Springer, 2015.
[46] C. Martin, T. Pham, W. Sun, Significant differences in the material properties between aged human and porcine aortic tissues, Eur. J. Cardio-thorac. Surg.: Off. J. Eur. Assoc. Cardio-thorac. Surg. 40 (1) (2011) 28–34.
[47] T. Pham, W. Sun, Comparison of biaxial mechanical properties of coronary sinus tissues from porcine, ovine and aged human species, J. Mech. Behav. Biomed. Mater. 6 (2012) 21–29.
[48] S.L.Y. Woo, K.J. Ohland, J.A. Weiss, Aging and sex-related changes in the biomechanical properties of the rabbit medial collateral ligament, Mech. Ageing Dev. 56 (2) (1990) 129–142.
[49] R.L. Kwan, Y.P. Zheng, G.L. Cheing, The effect of aging on the biomechanical properties of plantar soft tissues, Clin. Biomech. (Bristol, Avon) 25 (6) (2010) 601–605.
[50] A.J. Wilson, G.B. Sands, I.J. LeGrice, A.A. Young, D.B. Ennis, Myocardial mesostructure and mesofunction, Am. J. Physiol.-Heart Circul. Physiol. 323 (2) (2022) H257–H275.
[51] V. Caorsi, C. Toepfer, M.B. Sikkel, A.R. Lyon, K. MacLeod, M.A. Ferenczi, Non–linear optical microscopy sheds light on cardiovascular disease, PLoS One 8 (2) (2013) e56136.
[52] G. Sommer, A.J. Schriefl, M. Andra, M. Sacherer, C. Viertler, H. Wolinski, G.A. Holzapfel, Biomechanical properties and microstructure of human ventricular myocardium, Acta Biomater. 24 (2015) 172–192.
[53] H. Liu, W. Qin, Z. Ma, B.Z. Gao, Y. Shao, T. Ye, T.K. Borg, Myofibrillogenesis in live neonatal cardiomyocytes observed with hybrid two-photon excitation fluorescence-second harmonic generation microscopy, J. Biomed. Opt. 16 (12) (2011) 126012.
[54] H. Liu, Y. Shao, W. Qin, R.B. Runyan, M. Xu, Z. Ma, T.K. Borg, R. Markwald, B.Z. Gao, Myosin filament assembly onto myofibrils in live neonatal cardiomyocytes observed by TPEF-SHG microscopy, Cardiovasc. Res. 97 (2) (2013) 262–270.
[55] P.J. Campagnola, L.M. Loew, Second-harmonic imaging microscopy for visualizing biomolecular arrays in cells, tissues and organisms, Nat. Biotechnol. 21 (11) (2003) 1356–1360.
[56] P.J. Campagnola, M.D. Wei, A. Lewis, L.M. Loew, High-resolution nonlinear optical imaging of live cells by second harmonic generation, Biophys. J. 77 (6) (1999) 3341–3349.
[57] F. Ahmad, S. Soe, N. White, R. Johnston, I. Khan, J. Liao, M. Jones, R. Prabhu, I. Maconochie, P. Theobald, Region-Specific Microstructure in the Neonatal Ventricles of a Porcine Model, Ann. Biomed. Eng. 46 (12) (2018) 2162–2176.
[58] B. Aigner, S. Renner, B. Kessler, N. Klymiuk, M. Kurome, A. Wünsch, E. Wolf, Transgenic pigs as models for translational biomedical research, J. Mol. Med. 88 (7) (2010) 653–664.
[59] A. Bassols, C. Costa, P.D. Eckersall, J. Osada, J. Sabria, J. Tibau, The pig as an animal model for human pathologies: a proteomics perspective, Proteom.–Clin. Appl. 8 (9–10) (2014) 715–731.
[60] Y. Luo, L. Lin, L. Bolund, T.G. Jensen, C.B. Sørensen, Genetically modified pigs for biomedical research, J. Inherit. Metab. Dis. 35 (4) (2012) 695–713.
[61] S. Dokos, B.H. Smaill, A.A. Young, I.J. LeGrice, Shear properties of passive ventricular myocardium, Am. J. Physiol.-Heart Circ. Physiol. 283 (6) (2002) H2650–H2659.
[62] A.J. Schriefl, H. Wolinski, P. Regitnig, S.D. Kohlwein, G.A. Holzapfel, An automated approach for three-dimensional quantification of fibrillar structures in optically cleared soft biological tissues, J. R. Soc., Interface 10 (80) (2013) 20120760.
[63] G. Sommer, D. Haspinger, M. Andrä, M. Sacherer, C. Viertler, P. Regitnig, G.A. Holzapfel, Quantification of shear deformations and corresponding stresses in the biaxially tested human myocardium, Ann. Biomed. Eng. 43 (10) (2015) 2334–2348.
[64] R.S. Kirton, A.J. Taberner, P.M. Nielsen, A.A. Young, D.S. Loiselle, Effects of BDM, $[Ca^{2+}]o$, and temperature on the dynamic stiffness of quiescent cardiac trabeculae from rat, Am. J. Physiol. Heart Circ. Physiol. 288 (4) (2005) H1662–H1667.
[65] Z.Q. Liu, Scale space approach to directional analysis of images, Appl. Opt. 30 (11) (1991) 1369–1373.
[66] N. Reznikov, R. Almany-Magal, R. Shahar, S. Weiner, Three-dimensional imaging of collagen fibril organization in rat circumferential lamellar bone using a dual beam electron microscope reveals ordered and disordered sub-lamellar structures, Bone 52 (2) (2013) 676–683.
[67] N. Reznikov, R. Shahar, S. Weiner, Three-dimensional structure of human lamellar bone: the presence of two different materials and new insights into the hierarchical organization, Bone 59 (2014) 93–104.
[68] L.L. Demer, F.C. Yin, Passive biaxial mechanical properties of isolated canine myocardium, J. Physiol. 339 (1983) 615–630.
[69] J.D. Humphrey, R.K. Strumpf, F.C. Yin, Biaxial mechanical behavior of excised ventricular epicardium, Am. J. Physiol. 259 (1 Pt 2) (1990) H101–H108.
[70] T. Pham, F. Sulejmani, E. Shin, D. Wang, W. Sun, Quantification and comparison of the mechanical properties of four human cardiac valves, Acta Biomater. 54 (2017) 345–355.
[71] T. Pham, W. Sun, Material properties of aged human mitral valve leaflets, J. Biomed. Mater. Res. A 102 (8) (2014) 2692–2703.
[72] P. Haynes, K.E. Nava, B.A. Lawson, C.S. Chung, M.I. Mitov, S.G. Campbell, A.J. Stromberg, S. Sadayappan, M.R. Bonnell, C.W. Hoopes, K.S. Campbell, Transmural heterogeneity of cellular level power output is reduced in human heart failure, J. Mol. Cell. Cardiol. 72 (2014) 1–8.
[73] J.E. Stelzer, H.S. Norman, P.P. Chen, J.R. Patel, R.L. Moss, Transmural variation in myosin heavy chain isoform expression modulates the timing of myocardial force generation in porcine left ventricle, J. Physiol. 586 (21) (2008) 5203–5214.
[74] J. van der Velden, L.J. Klein, M. van der Bijl, M.A.J.M. Huybregts, W. Stooker, J. Witkop, L. Eijsman, C.A. Visser, F.C. Visser, G.J.M. Stienen, Isometric tension development and its calcium sensitivity in skinned myocyte-sized preparations from different regions of the human heart, Cardiovasc. Res. 42 (3) (1999) 706–719.
[75] H. Wang, X. Zhang, S.M. Dorsey, J.R. McGarvey, K.S. Campbell, J.A. Burdick, J.H. Gorman III, J.J. Pilla, R.C. Gorman, J.F. Wenk, Computational investigation of transmural differences in left ventricular contractility, J. Biomech. Eng. 138 (11) (2016) 114501.
[76] L. Mullins, N. Tobin, Theoretical model for the elastic behavior of filler-reinforced vulcanized rubbers, Rubber Chem. Technol. 30 (2) (1957) 555–571.
[77] J.L. Emery, J.H. Omens, A.D. McCulloch, Strain softening in rat left ventricular myocardium, J. Biomech. Eng. 119 (1) (1997) 6–12.
[78] J.B. Caulfield, T.K. Borg, The collagen network of the heart, Lab. Invest. 40 (3) (1979) 364–372.
[79] P.C. McDonald, J.E. Wilson, S. McNeill, M. Gao, J.J. Spinelli, F. Rosenberg, H. Wiebe, B.M. McManus, The challenge of defining normality for human mitral and aortic valves: geometrical and compositional analysis, Cardiovasc. Pathol. Off. J. Soc. Cardiovasc. Pathol. 11 (4) (2002) 193–209.
[80] K.T. Weber, W.A. Clark, J.S. Janicki, S.G. Shroff, Physiologic versus pathologic hypertrophy and the pressure-overloaded myocardium, J. Cardiovasc. Pharmacol. 10 (Suppl 6) (1987) S37–S50.
[81] K.T. Weber, J.S. Janicki, S.G. Shroff, R. Pick, R.M. Chen, R.I. Bashey, Collagen remodeling of the pressure-overloaded, hypertrophied nonhuman primate myocardium, Circ. Res. 62 (4) (1988) 757–765.
[82] Y. Fung, in: Biomechanical Aspects of Growth and Tissue Engineering, Springer, Biomechanics, 1990, pp. 499–546.
[83] J.D. Humphrey, Cardiovascular Solid Mechanics: Cells, Tissues, and Organs, Springer Science & Business Media, 2013.
[84] D.D. Streeter Jr, D.L. Bassett, An engineering analysis of myocardial fiber orientation in pig's left ventricle in systole, Anat. Rec. 155 (4) (1966) 503–511.
[85] A.J. Pope, G.B. Sands, B.H. Smaill, I.J. LeGrice, Three-dimensional transmural organization of perimysial collagen in the heart, Am. J. Physiol.-Heart Circ. Physiol. 295 (3) (2008) H1243–H1252.
[86] R.M. Smith, A. Matiukas, C.W. Zemlin, A.M. Pertsov, Nondestructive optical determination of fiber organization in intact myocardial wall, Microsc. Res. Tech. 71 (7) (2008) 510–516.
[87] D.D. Streeter Jr., H.M. Spotnitz, D.P. Patel, J. Ross Jr., E.H. Sonnenblick, Fiber orientation in the canine left ventricle during diastole and systole, Circ. Res. 24 (3) (1969) 339–347.
[88] K.T. Weber, Y. Sun, S.C. Tyagi, J.P. Cleutjens, Collagen network of the myocardium: function, structural remodeling and regulatory mechanisms, J. Mol. Cell. Cardiol. 26 (3) (1994) 279–292.
[89] M.L. Burgess, J.C. McCrea, H.L. Hedrick, Age-associated changes in cardiac matrix and integrins, Mech. Ageing Dev. 122 (15) (2001) 1739–1756.
[90] K. Weber, J. Janicki, S. Shroff, R. Pick, C. Abrahams, R. Chen, Collagen compartment remodeling in the pressure overloaded left ventricle, J. Appl. Cardiol. 3 (1) (1988) 37–46.
[91] R. Dawson, G. Milne, R.B. Williams, Changes in the collagen of rat heart in copper-deficiency-induced cardiac hypertrophy, Cardiovasc. Res. 16 (10) (1982) 559–565.
[92] S. Factor, T. Robinson, R. Dominitz, S. Cho, Alterations of the myocardial skeletal framework in acute myocardial infarction with and without ventricular rupture. A preliminary report, Am. J. Cardiovasc. Pathol. 1 (1) (1987) 91–97.
[93] F. Ahmad, R.j. Prabhu, J. Liao, S. Soe, M.D. Jones, J. Miller, P. Berthelson, D. Enge, K.M. Copeland, S. Shaabeth, R. Johnston, I. Maconochie, P.S. Theobald, Biomechanical properties and microstructure of neonatal porcine ventricles, J. Mech. Behav. Biomed. Mater. 88 (2018) 18–28.
[94] F.E. Rademakers, M.B. Buchalter, W.J. Rogers, E.A. Zerhouni, M.L. Weisfeldt, J.L. Weiss, E.P. Shapiro, Dissociation between left ventricular untwisting and filling. Accentuation by catecholamines, Circulation 85 (4) (1992) 1572–1581.
[95] S.-J. Dong, P.S. Hees, C.O. Siu, J.L. Weiss, E.P. Shapiro, MRI assessment of LV relaxation by untwisting rate: a new isovolumic phase measure of τ, Am. J. Physiol.-Heart Circ. Physiol. 281 (5) (2001) H2002–H2009.
[96] G.A. Holzapfel, R.W. Ogden, Constitutive modelling of passive myocardium: a structurally based framework for material characterization, Philos. Trans. R. Soc. A: Math., Phys. Eng. Sci. 367 (1902) (2009) 3445–3475.